

**University of Alberta**

**Vibrational Absorption, Vibrational Circular Dichroism and Theoretical  
Studies of Methyl Lactate Molecules in Solution Phase and in Argon  
Matrices**

by

**Yang Liu**

A thesis submitted to the Faculty of Graduate Studies and Research  
in partial fulfillment of the requirements for the degree of

**Master of Science**

Department of Chemistry

©Yang Liu

Spring 2011

Edmonton, Alberta

Permission is hereby granted to the University of Alberta Libraries to reproduce single copies of this thesis and to lend or sell such copies for private, scholarly or scientific research purposes only. Where the thesis is converted to, or otherwise made available in digital form, the University of Alberta will advise potential users of the thesis of these terms.

The author reserves all other publication and other rights in association with the copyright in the thesis and, except as herein before provided, neither the thesis nor any substantial portion thereof may be printed or otherwise reproduced in any material form whatsoever without the author's prior written permission.

## **Examining Committee**

Prof. Yunjie Xu, Chemistry

Prof. John Klassen, Chemistry

Prof. Frank A. Hegmann, Physics

**Dedicated to those I most loved**

Mother: Mijie Wang

Father: Zhiyi Liu

Wife: Xiao Xing

## Abstract

The infrared vibrational absorption (VA) and vibrational circular dichroism (VCD) spectra of methyl lactate in carbon tetrachloride and methanol have been measured in the 1000-1800  $\text{cm}^{-1}$  region. Noticeable changes due to the solute self-aggregation and solvent-solute intermolecular hydrogen-bonding in the reported spectra have been detected. A series of density functional theory (DFT/B3LYP/6-311++G\*\*) and single point MP2/6-311++G\*\* energy calculations have been performed to identify and to model the explicit hydrogen-bonded complex. Geometry search and optimization have been performed for the most stable conformers. The VA and VCD spectra of these complexes have been simulated and compared with the corresponding experimental spectra. A novel experimental apparatus has been set up in order to carry out Fourier transform infrared-VCD measurements in cold rare gas matrices. Some preliminary results obtained with this new setup and the challenges in these experiments are discussed.

## Acknowledgements

First and foremost, I would like to express my deep and sincere gratitude to my supervisor, Dr. Yunjie Xu for her guidance and encouragement during my graduate school. I clearly remembered the time when I was very confused and puzzled in my life after I just finished my undergraduate school. Dr. Xu was very patient and supportive and gave many suggestions on how to choose a career pathway according to my academic background. After the past few years training, her wide knowledge, logic way of thinking and constructive comments have made my graduate school life very rewarding in the end.

I would like also to show my warm thanks to the previous group members Dr. Gunchun Yang and Dr. Martin Losada. They were very friendly to help me answer endless questions about theoretical calculations and research methods. In particular, I also want to thank Shawn(Xunchen) Liu, Tobby (Tao) Zeng, Connie(Peiyan) Zhu, Dr. Fumei Sunahori and Javix Thomas. I had many remembering scientific discussions with them, which really enlightened my way of thinking in research. They have been very good friends both in research and in personal life. I would also like to thank Dr. Wolfgang Jäger's group for their generous help in many occasions. A particular note of thanks has to give to our many staff members in the machine shop. They have been very helpful in helping me to design the Matrix isolation system and trouble shoot the instrumental

problems.

I am greatly indebted to my parents for their belief in me. They have been understanding and encouraging with endless love throughout my life. In the end, I want to thank my wife who gives me her absolute support and caring. Without her it would be impossible to finish this thesis.

# Table of contents

Chapter	Page
<b>Chapter 1 Introduction</b> .....	1
References.....	9
<b>Chapter 2 Theoretical methods and experimental approaches</b> .....	11
2.1 Theoretical background.....	11
2.2 <i>ab initio</i> calculations.....	14
2.3 Experimental approaches.....	16
2.3.1 IR module.....	16
2.3.2 VCD module.....	19
2.4 Matrix isolation system.....	23
References.....	26
<b>Chapter 3 Study of methyl lactate self-aggregation and methyl methanol lactate-intermolecular interactions</b> .....	28
3.1 Introduction.....	28
3.2 Experimental.....	32
3.3 Computation methods.....	33
3.3.1 MD simulation.....	33
3.3.2 <i>ab initio</i> calculation.....	34
3.4 Results and discussion.....	35
3.4.1 Experimental VA and VCD spectra of ML in methanol and in carbon tetrachloride.....	35

3.4.2 Simulations of the VA and VCD spectra of ML in methanol and CCl <sub>4</sub> .....	39
3.4.2.1 Coordination number of the first methanol shell and the degree of ML self-aggregation in methanol.....	40
3.4.2.2 Dimer or larger self-aggregation ML clusters in CCl <sub>4</sub> .....	44
3.4.2.3 The 1:1, 1:2, and 1:3 ML-methanol clusters and the ML dimers..	46
3.4.3 Comparison of the experimental and simulated VA and VCD spectra...	53
3.5 Conclusion.....	59
References.....	60

**Chapter 4 VCD spectroscopy of chiral molecular system in cold rare gas matrices.....63**

4.1 Introduction.....	63
4.1.1 Introduction to some general properties of rare gas matrices.....	63
4.1.1.1 Purity.....	64
4.1.1.2 Transparency.....	66
4.1.1.3 Inertness.....	67
4.1.1.4 Rigidity.....	67
4.1.1.5 Volatility.....	69
4.1.1.6 Heat of fusion and lattice energy.....	70
4.1.1.7 Thermal conductivity.....	72
4.1.1.8 Crystal structures.....	74
4.1.2 Previous VCD measurements in matrices and experimental challenges.....	78
4.2 Experiments and Discussions.....	82
4.3 Concluding remarks.....	88

References.....90

**Chapter 5 General Conclusion.....91**

# List of Tables

Table	Page
3-1 Observed fundamental VA bands for ML in the CCl <sub>4</sub> , methanol and water solvents. All frequencies are in cm <sup>-1</sup> .....	37
3-2 The raw dissociation energies ( <i>De</i> ), the BSSE and ZPE corrections, the corrected dissociation energies ( <i>Do</i> ), and the relative dissociation energies ( $\Delta Do$ ) of ML monomers and ML-methanol complexes at the B3LYP/6-311++G** and the MP2/6-311++G** level of theory. All energy values are in kcal mol <sup>-1</sup> .....	49
4-1 Typical research grade gases Ar, N <sub>2</sub> and O <sub>2</sub> and their respective major impurities in unit of ppm. ....	65
4-2 Thermal properties of some common matrix materials.....	68
4-3 The temperatures of some common matrix materials at the vapor pressure of 100 mTorr.....	70
4-4 Heat of fusion and lattice energies of some common matrix materials.....	72
4-5 Thermal conduction properties of some common matrix materials.....	73
4-6 Trapping site diameters (10 <sup>-10</sup> m) for some common matrix materials at 4K.....	78

# List of Figures

Table	Page
2-1 The simplified schematics of a general Michelson interferometer illuminated by a light source.....	17
2-2 The transmission curve of BaF <sub>2</sub> in the spectral range from 4000 to 500cm <sup>-1</sup> .....	18
2-3 The transmission curve of CaF <sub>2</sub> at the spectral range from 4000 to 500cm <sup>-1</sup> .....	19
2-4 Right circularly polarized light with generated by between the two linearly polarized lights (blue and green) with a 90 degree phase difference.....	21
2-5 Left circularly polarized light generated by the two linearly polarized lights (blue and green) with a 270 degree phase difference.....	21
2-6 The general layout of FTIR-VCD spectrometer.....	23
2-7 The schematics of FT-VCD coupled with matrix isolation system.....	24
3-1 Atom labelling for both ML and methanol. The dominant conformer of ML which has ~90% of the monomer population is shown.....	30
3-2 The experimental VA and VCD spectra of 0.2 M and 2M ML in CCl <sub>4</sub> and 2M ML in methanol. The solid line (—) in the VCD spectra is for (R)-ML while the dotted line (---) is for (S)-ML.....	36
3-3 RDFs obtained from the MD simulation of 2M ML in methanol. The RDFs shown are related to the intermolecular interactions between ML and methanol. See Figure 3.1 for atom labelling of ML and methanol.....	41
3-4 RDFs obtained from the MD simulation of 2M ML in methanol. The RDFs shown are related to the self-aggregation of ML in methanol. See Figure 3.1 for atom labelling of ML and methanol.....	43
3-5 RDFs obtained from the MD simulation of 2M ML in CCl <sub>4</sub> . The RDFs shown are related to the self-aggregation of ML in CCl <sub>4</sub> . See Figure 3.1 for	

atom labelling of ML.....	45
3-6 Optimized geometries of the seven most stable 1:1 ML-methanol conformers and the two ML dimers. The intermolecular and intramolecular hydrogen bond lengths are in the unit of Å.....	48
3-7 Optimized geometries of the six most stable 1:2 ML-methanol conformers. The intermolecular and the (secondary) intramolecular hydrogen bond lengths are in the unit of Å.....	52
3-8 Optimized geometries of the six most stable 1:3 ML-methanol conformers. The intermolecular and the (secondary) intramolecular hydrogen bond lengths are in the unit of Å. Any potential secondary intramolecular hydrogen bond with a length longer than ~3 Å is not shown.....	53
3-9 Calculated population weighted VA and VCD spectra of the ML monomer, the ML dimer, and the ML-(methanol) <sub>1,2,3</sub> clusters, at the B3LYP/6-311+G** level of theory. The Boltzmann factors calculated from the single point MP2 energies are used for the population weights.....	56
3-10 Comparison of the experimental VA and VCD spectra of the 2 M ML in methanol with the corresponding population weighted VA and VCD spectra of 15% ML monomer, 55% ML-1m, and 30% ML-3m (top). Comparison of the experimental VA and VCD spectra of the 2 M ML in CCl <sub>4</sub> with the corresponding population weighted VA and VCD spectra of 65% ML monomer and 35% ML-ML (bottom).....	58
4-1 The graphical demonstration shows how the matrix material condense on the cold plate.....	74
4-2 Hexagonal close-packed structure lattice of noble gas.....	75
4-3 The structure of cubic close-packed structure lattice of noble gas.....	76
4-4 The structures of substitutional holes, tetrahedral holes and octahedral holes.....	77
4-5 Three spectra of MI-IR experiments with cryostat at room temperature, 13K in ultrahigh vacuum condition and with argon deposition for 2 hours to demonstrate the how dry the agon gas after introducing the drying bottle.....	83

4-6 The spectra are divided into three regions:  $2500\text{cm}^{-1}$ - $3700\text{cm}^{-1}$ ,  $1000\text{cm}^{-1}$ - $1850\text{cm}^{-1}$  and  $1100\text{cm}^{-1}$  - $600\text{cm}^{-1}$ . The spectra on the left is from literature and on the right is from my experiments. (the left part of the figures is taken from the references 8 for comparison).....85

# Chapter 1 Introduction

In 1884 Baltimore Lectures, Lord Kelvin first defined chirality: "I call any geometrical figure, or group of points, chiral, and say that it has chirality, if its image in a plane mirror, ideally realized, cannot be brought to coincide with itself." In nature, from simple carbohydrates to large biomolecules, one stunning fact is that nearly all of them possess chirality. Chirality is also termed handedness since our hands are the most common example of a pair of chiral entity. Chiral objects can recognize each other specifically. For example, a hand shake between two right hands feel right, while that between a right and a left hand feel awkward. This is a macroscopic example of chirality recognition. In 1894 Fisher postulated the famous "lock and key" principle to explain the specific recognition between enzyme and substrate in biochemical reactions.<sup>1</sup> Such a metaphor displays a vivid picture of the specific recognition. Since then, there have been substantial research efforts to understand such recognition processes at the microscopic level in order to quantify the intermolecular interactions involved quantitatively.<sup>2</sup>

A step further in this research direction is to consider the effects of environment, such as solvent effects, in a chirality recognition process since nearly all important biological events and many enantio-selective chemical reactions happen in solution. This is one reason for me to study intermolecular interactions, in particular, hydrogen-bonding interactions between methanol and

methyl lactate, a prototype chiral molecule in my thesis work.

Chirality plays a particularly important role in pharmaceutical industry since enantiomers of a drug may have distinctive different activities in biological functions. Two better know examples are Thalidomide and Citalopram. Thalidomide was introduced as a sedative drugs and sold in many countries from 1957 to 1961 for treatment of morning sickness in pregnant women. The severe side effects caused more than 10,000 birth defects and it is called "one of the biggest medical tragedies in modern times".<sup>3</sup> It is the S-enantiomer which causes severe side effects such as teratogenicity and neuropathy, whereas the R-enantiomer is the effective ingredient, although racemization takes place in vivo. Citalopram is an antidepressant drug and its S-enantiomer is 30-fold more effective than the R-enantiomer. Although it is not mandatory in the United States or Europe to develop single enantiomeric drugs exclusively, it is now mandatory to establish the toxicity and effectiveness separately for all drug candidates. By 2003, more than 50% drugs are single-enantiomers and more single enantiomeric drugs are being submitted for approval.<sup>4</sup> There is therefore high demand for a robust and convenient method for the determination of absolute configuration of chiral molecules in vivo such as in solution directly. Vibrational circular dichroism (VCD) spectroscopy has emerged in recent years as such a promising new method for the absolute configuration determination of chiral molecules in solution. This is the second motivation for my thesis work where I apply VCD

spectroscopy and focus on how the solvent like methanol can affect the conformation of methyl lactate in solution. Furthermore, I try to understand how such solvent effects can affect the interpretation of the chiroptical spectra observed to extract information about the absolute configuration of the targeted chiral molecule.

X-ray crystallography is a very powerful and most used method currently for absolute configuration determination, although it requires a single crystal sample.<sup>5</sup> To investigate the chirality-sensitive optical properties of chiral molecules, the most common known methods are optical rotation and electronic circular dichroism (ECD). Optical rotatory dispersion (ORD) spectroscopy is based on differences of refractive indices for the left and right circular polarized light, whereas the ECD originates from the differential absorptions of the left and right circular polarized light accompanying an electronic transition. The French scientist Cotton first discovered the CD effect in 1895. So it is also called Cotton Effect. But its application to characterize the chiral organic molecules didn't rise to prominence until the major instrumentation advance in 1950s and 1960s.<sup>6,7</sup> In the 1970s, a few researchers started to extend the ORD and CD to the infrared region where most fundamental vibrational transitions lie.<sup>8,9</sup> Although these initial efforts were not successful because the magnitude of VCD signals is quite small, they stimulated experimental spectroscopists to look for better material for optical components and new spectroscopic instrument designs. The major breakthrough

came in early 1970s when the ZnSe birefringent material was used to construct photoelastic modulator, an essential optical component for generating modulating circularly polarized light, with a wavenumber cut off reach as low as 650  $\text{cm}^{-1}$ .<sup>10</sup> This starts the era of VCD spectroscopy, albeit early publications on VCD<sup>11,12</sup> are not ideal in terms of frequency range coverage and sensitivity. In 1980s, Nafie group first implemented the Fourier transform infrared (FTIR) technology in the VCD spectrometry.<sup>13,14,15</sup> This original design, together with several major improvements, are now implemented in the current commercially available FTIR-VCD spectrometers which are sold by almost all major FTIR spectrometer companies such as Bruker, Bomen (BioTools), and Nicolet. These spectrometer are widely used in academic researches and in pharmaceutical industries.<sup>16</sup>

In order to extract the absolute structural information, one needs to compare the theoretically simulated VCD spectra with the experimental spectral data. In the early days, some empirical rules based on collections of similar chiral molecules with their absolute configurations established by other methods were used. This practice often results in uncertain or erratic interpretations. Considerable research efforts had been put into developing robust and accurate theoretical methods to calculate VCD spectra. One significant challenge is that the electronic contribution to the magnetic transition dipole moment vanishes within the Born-Oppenheimer approximation since one needs to take a derivative of the magnetic transition dipole moment operator with respect to the time derivative of

the normal vibrational coordinate ( $Q_j$ ).<sup>17</sup> To overcome this problem, a number of models were postulated, which did not consider the electronic wave functions explicitly, but they didn't arrive at a general equation which works for all cases and the results are unsatisfying. Models considering the electronic wave functions explicitly such as localized molecular orbital,<sup>18</sup> vibronic coupling,<sup>19</sup> nuclear electric shielding tensor<sup>20</sup> were also proposed. These all contain the summation over the complete set of the excited electronic states adiabatically. In practice, the invocation of average-energy approximations or the drastic truncation of summation generally led to less than satisfying results. Craig and Thirunamachandran, Nafie and Freedman, and many other groups had developed several theoretical methods in the 80s and 90s to introduce corrections to the BO approximation in order to better evaluate the electronic contribution to a vibrational magnetic dipole transition moment. In mid 80s, Buckingham together with his co-workers at Oxford University and Stephens at the University of Southern California<sup>17</sup> independently proposed to use the so-called magnetic field perturbation (MFP) method. In this approach, it is only necessary to evaluate the ground state wave function as a function of nuclear displacement and of applied magnetic field and no need to do the summation over all excited electronic states. In 1996, Stephens and his co-workers applied the MFP method together with the density functional theory<sup>21</sup> to calculate VCD spectra which compared favorably with the experimental ones. This approach was eventually implemented in

Gaussian95, Package of programs<sup>22</sup> and is still the method used for VCD calculation in Gaussian09.<sup>23</sup>

Last ten year has witnessed substantial advances in both the experimental and theoretical development of VCD spectroscopy. It has now become a powerful method for absolute configuration determination of chiral molecules. Furthermore, VCD is often very sensitive to the changes in dihedral angles and conformational changes can sometimes generate the opposite VCD sign. In addition, the solute-solute and the solute-solvent interactions, especially hydrogen-bonding interactions can cause changes in conformational geometry and relative distribution, in vibrational band frequency and intensity, as well as VCD pattern. The first main part of my research work focuses on understanding these effects using methyl lactate in methanol as the model molecular system. Methyl lactate was chosen as the target molecule because of it has several important functional groups and is a relative small molecular size. The latter makes it amenable to high level ab initio calculations. Interestingly methyl lactate itself is also used in industry as an environmental friendly alternative solvent to the toxic and polluting organic solvents.<sup>24</sup>

In the second project, I set up a cold rare gas matrix isolation system and combine it with the FTIR-VCD spectrometer to conduct MI-VCD experiments for methyl lactate and methyl lactate-methanol, or water complexes. Matrix isolation system is defined as a sytem where the guest molecules are completed separated

by other host molecules and condensed on an optic through a cryogenic device. As mentioned above, solute-solvent interactions can have severe effects on the VCD spectra obtained. Sometimes, such effects may lead to a blurry and featureless spectrum and very limited information can be extracted. The first MI-VCD experiment was reported by Stephen group and Polavarapu groups. Their experiments involved only rigid and single conformational chiral molecules, such as pinene and propylene oxide. In 1996, Jalkanene and Suhai group<sup>25</sup> first suggested coupling the VCD and matrix isolation to study conformational flexible molecules in order to better compare with the corresponding theoretical simulations. This approach has recently been demonstrated for (R)-alaninol, a highly flexible system.<sup>26</sup> Without the solvent broadening and rotameric averaging in a cold rare gas matrix, a much better spectral resolution was achieved and the resulting spectra could be compared to the simulation more conclusively. Another reason to use the cold rare gas matrix is to have some control over the sample composition, for example to make dominantly binary complexes rather than higher clusters. We hope to be able to better separate a particular size of clusters so that one can resolve their spectral features separately.

The rest of my thesis are organized into three chapters. Chapter 2 contains some brief reviews of the basics of VCD instrument and theory and of matrix isolation technique, and the related ab initio calculations. Chapter 3 presents the published paper on the VCD studies of methyl lactate in methanol. Chapter 4

discusses the matrix isolation-VCD (MI-VCD) experiments I have developed so far, together with some important points on how to prepare a cold rare gas matrix for VCD measurements and on where the main artifacts associated in the raw experimental data are from.

During my thesis study, I was also involved in such a project to determine the absolute structure of several novel carbohydrates synthesized by Professor Todd Lowary and his research group. This resulted in a publication with me as the third co-author.<sup>27</sup> This work is not included in the current thesis.

## References:

- 1 Fisher, E. *Ber. Dtsch. Chem. Ges.* **1984**, 27, 2985.
- 2 Schneider, H. J. *Methods and Principles in Medicinal Chemistry*, **2003**, 19, 21.
- 3 <http://en.wikipedia.org/wiki/Thalidomide>
- 4 McConathy, J. *Primary Care Companion J. Clin. Psychiatry*, **2003**, 5, 70.
- 5 Stephens, P. J.; Devlin, F. J.; Pan, J. J. *Chirality*, **2008**, 20, 643.
- 6 Crabbe, P. *Angewandte Chemie*, **1966**, 78, 399.
- 7 Velluz, L.; LeGrand, M.; Grosjean, M. *Angewandte Chemie*, **1965**, 4, 898.
- 8 Wyss, H. R.; Gunthard, H. H. *Helv. Chim. Acta.* **1966**, 49, 660.
- 9 Wyss, H. R.; Gunthard, H. H. *J. opt. soc. Am.* **1966**, 56, 888.
- 10 Cheng, J. C.; Nafie, L. A.; Allen, S. D.; Braunstein, A. I. *Appl. Optics.* **1976**, 15, 1960.
- 11 Nafie, L. A.; Cheng, J. C.; Stephens, P. J. *J. Am. Chem. Soc.* **1975**, 97, 3842.
- 12 Keiderling, T. A.; Stephen, P. J. *J. Am. Chem. Soc.* **1977**, 99, 8061.
- 13 Nafie, L. A.; Diem, M. *Appl. Spectrosc.* **1979**, 33, 130.
- 14 Nafie, L. A.; Diem, M.; Vidrine, D. W. *J. Am. Chem. Soc.* **1979**, 101, 496.
- 15 Lipp, E. D.; Zimba, C. G.; Nafie, L. A. *Chem. Phys. Lett.* **1982**, 90, 1.
- 16 Dukor, R. K.; Nafie, L. A. *Encyclopedia of analytical chemistry: instrumentation and applications*, John Wiley & Sons: Chichester, UK, **2000**, p 662.
- 17 Stephens, P. J. *J. Phys. Chem.* **1985**, 89, 748.
- 18 (a) Nafie, L. A.; Walnut, T. H. *Chem. Phys. Lett.* **1977**, 49, 441. (b) Walnut, T. H. Nafie, L. A. *Chem. Phys.* **1977**, 67, 1501.
- 19 (a) Nafie, L. A.; Freedman, T. B. *J. Phys. Chem.* **1983**, 78, 7108. (b) Dutler, R.; Rauk, A. *J. Am. Chem. Soc.* **1989**, 111, 6957. (c) Yang, D.; Rauk, A. *J. Chem. Phys.* **1992**, 97, 6517.

- 20 (a) Hunt, K. L. C.; Harris, R. A. *J. Chem. Phys.* **1991**, *94*, 6995. (b) Lazzeretti, P.; Malagoli, M.; Zanasi, R. *Chem. Phys. Lett.* **1991**, *179*, 297.
- 21 Tom, Z. *Chem. Rev.* **1991**, *91*, 651.
- 22 Frisch, M. J.; Trucks, G. W.; Schlegel, H. B.; Gill, P. M. W.; Johnson, B. G.; Robb, M. A.; Cheeseman, J. R.; Keith, T.; Peterson, G. A.; Montgomery, J. A.; Raghavachari, K.; Al-Laham, M. A.; Zakrzewski, V. G.; Ortiz, J. V.; Foresman, J. B.; Cioslowski, J.; Stefano, B. B.; Nanayakkara, A.; Challacombe, M.; Peng, C. Y.; Ayala, P. Y.; Chen, W.; Wong, M. W.; Andres, J. L.; Replogle, E. S.; Gomperts, R.; Martin, R. L.; Fox, D. J.; Binkley, J. S.; Defrees, D. J.; Baker, J.; Stewart, J. P.; Head-Gordon, M.; Gonzalez, C.; Pople, J. A. GAUSSIAN 95, Development Version; Gaussian, Inc.: Pittsburgh, PA, **1995**.
- 23 Gaussian 09, Revision A.1, Frisch, M. J.; Trucks, G. W.; Schlegel, H. B.; Scuseria, G. E.; Robb, M. A.; Cheeseman, J. R.; Scalmani, G.; Barone, V.; Mennucci, B.; Petersson, G. A.; Nakatsuji, H.; Caricato, M.; Li, X.; Hratchian, H. P.; Izmaylov, A. F.; Bloino, J.; Zheng, G.; Sonnenberg, J. L.; Hada, M.; Ehara, M.; Toyota, K.; Fukuda, R.; Hasegawa, J.; Ishida, M.; Nakajima, T.; Honda, Y.; Kitao, O.; Nakai, H.; Vreven, T.; Montgomery, Jr., J. A.; Peralta, J. E.; Ogliaro, F.; Bearpark, M.; Heyd, J. J.; Brothers, E.; Kudin, K. N.; Staroverov, V. N.; Kobayashi, R.; Normand, J.; Raghavachari, K.; Rendell, A.; Burant, J. C.; Iyengar, S. S.; Tomasi, J.; Cossi, M.; Rega, N.; Millam, N. J.; Klene, M.; Knox, J. E.; Cross, J. B.; Bakken, V.; Adamo, C.; Jaramillo, J.; Gomperts, R.; Stratmann, R. E.; Yazyev, O.; Austin, A. J.; Cammi, R.; Pomelli, C.; Ochterski, J. W.; Martin, R. L.; Morokuma, K.; Zakrzewski, V. G.; Voth, G. A.; Salvador, P.; Dannenberg, J. J.; Dapprich, S.; Daniels, A. D.; Farkas, Ö.; Foresman, J. B.; Ortiz, J. V.; Cioslowski, J.; Fox, D. J. Gaussian, Inc., Wallingford CT, **2009**
- 24 Warner, J. C.; Cannon, A. S.; Dye, K. M. *Environ. Impact Asses. Rev.* **2004**, *24*, 775.
- 25 Jalkanen, K.; Suhai, S. *Chem. Phys.* **2008**, *357*, 116.
- 26 Gyorgy, T.; Gabor, M.; Elemer, V. *Angewandte Chemie*, **2006**, *118*, 1775.
- 27 Yang, G.; Li, J.; Liu, Y.; Lowary, T. L.; Xu, Y. *Organic & Biomolecular Chemistry* **2010**, *8*, 3777.

## Chapter 2 Theoretical methods and experimental approaches

The relevant theoretical and experimental methods to my thesis work are described in this chapter. First, the vibration and vibrational circular dichroism spectroscopy description in quantum chemistry are reviewed only briefly since no new theory has been developed in this thesis. Second, the suitable computational methods utilized in my thesis work using the standard electronic structural packages such as Gaussian03<sup>1</sup> are discussed. In the experimental part, I will go through the major parts of a Fourier transform IR- VCD spectrometer and the operating principles of a FTIR and a VCD module, and describe how to construct and to operate a matrix isolation system.

### 2.1 Theoretical background<sup>2</sup>

Consider a diatomic molecular system in the harmonic oscillator approximation, the following relationship holds:

$$\nu = \frac{1}{2\pi} \sqrt{\frac{k}{\mu}} \quad (2.1)$$

where  $\nu$  represents the frequency,  $\mu$  is the reduced mass, and  $k$  is the force constant. The corresponding vibrational energy of such a system is given by:

$$E_v = \eta \omega_e \left( v + \frac{1}{2} \right) \quad (2.2)$$

where the  $\omega_e$  is the equilibrium vibration frequency and  $v$  is the vibrational quantum number which can be 0 or any positive integers. Therefore the lowest vibrational energy, termed the zero point energy, is  $E_0 = \eta \omega_e / 2$ . The general requirement for an IR active vibrational transition is that the electric dipole moment of the molecule changes in the course of the vibrational motion. The vibrational quantum number  $v$  follows the selection rule  $\Delta v = \pm 1$ . The intensity of a vibrational transition from the ground vibrational level to the first excited vibrational level in the ground electronic state is:

$$D(g-e) = |\langle g | \hat{\mu}_{el} | e \rangle|^2 \quad (2.3)$$

where  $g$  represents the ground vibrational level,  $e$  means the first excited level, and  $\hat{\mu}_{el}$  is the electronic dipole moment operator.<sup>3</sup>

The vibration motions of a polyatomic molecule with  $N$  atoms can be treated as  $(3N-6)$  independent harmonic oscillators or  $(3N-5)$  harmonic oscillators for nonlinear or linear molecules, respectively. The  $v$  quantum number selection rule follows the same  $\Delta v = \pm 1$  as in the diatomic case. This selection rule results from the Hermite polynomials of Taylor's expansion when only the first order terms are considered. Therefore if the higher terms and the anharmonicity are considered, the selection rule relaxes to include  $\Delta v = \pm 2, 3, \dots$  terms. The first overtone band

is usually about  $\frac{1}{10}$  to  $\frac{1}{100}$  less intense than the fundamental band. Each vibrational level supports many rotational levels. However, these rotational substructures are typically not resolved in the condensed phase spectroscopy, such as those performed in solution and in matrices. Occasionally, one can observe the rough P, Q, and R branches of the vibrational bands, especially in the cold rare gas matrices.

VCD is the difference absorption of the left versus right circularly polarized light by a chiral sample accompany a vibrational transition. It can be expressed experimentally in terms of the difference in either absorbance or molar absorptivity if the pathlength and the concentration of a sample are known. The intensity of a VCD band is calculated with the following formula.

$$R(g - e) = \text{Im}[\langle g | \hat{\mu}_{el} | e \rangle] \bullet [\langle e | \hat{\mu}_{mag} | g \rangle] \quad (2.4)$$

where  $g$ ,  $e$ , and  $\hat{\mu}_{el}$  are defined the same as in equation (2.3) while  $\hat{\mu}_{mag}$  is the magnetic dipole moment operator and Im means imaginary.<sup>3</sup> In evaluating the magnetic dipole moment integral, the leading term includes taking a derivative with respect to nuclear velocity. This term would be zero within the Born-Oppenheimer (BO) approximation. Obviously, one needs to go beyond the BO approximation. A number of theoretical formalisms have been developed over the years to overcome this problem.<sup>3,4</sup> Currently, only the magnetic field perturbation (MFP) is implemented in Gaussian03 for VCD calculations.<sup>4</sup>

## 2.2 *Ab initio* calculations

High level *ab initio* calculations have been carried out in this thesis work to search possible conformational structures and to simulate the IR and VCD spectra of the targeted molecular systems. All calculations have been performed using Gaussian 03 package of programs. All geometry optimization calculations, harmonic frequency, and IR and VCD intensity calculations have been carried out using Density Functional Theory (DFT).<sup>5,6,7</sup> The molecule of interest, methyl lactate, has 4C, 3O and 8H, and its complexes with 1 to 3 methanol molecules have many more atoms. DFT is therefore a desirable method to carry out the extensive conformational search for all these systems since the computational cost is low compared to the wavefunction method such as the second order Moller-Plesset (MP2)<sup>8</sup> perturbation theory method and it provides adequate predictions to interpret the experimental observation for these mid-size molecules. The MP2 method treats electron correlation explicitly and is used to calculate the single point energy for the structural minima identified in the DFT search for comparison purpose.

It is important to apply the appropriate basis sets in these calculations. For molecules with strong polarization and diffusion, especially for hydrogen bonding complexes, it is unavoidable to use large basis sets, even though it will drastically increase the computational expenses compared to the relatively small basis sets. The types of basis sets used in this thesis are of Pople's Gaussian functions.<sup>9</sup> They

are hybrid type functions with different numbers of Gaussian functions to simulate the core electrons, intermediate electrons and valence electrons. Typically, I started out with a relatively small basis set to search for all the possible local minimum structures and then re-optimized them with the desirable larger basis set. The functional used is the very successful three-parameter hybrid functional B3LYP proposed by Becke,<sup>10,11</sup> which has been proven to be suitable for VCD calculations.

To evaluate the relative contribution from each conformer, it is necessary to find out their dissociation energy and their Boltzmann distribution at room temperature, i.e., the experimental temperature. In particular, the dissociation energy of a complex AB with two subunits A and B, is determined by subtracting energy of each subunit from the total complex energy.

$$E_{\text{int}} = E_{AB} - E_A - E_B \quad (2.5)$$

where the  $E_{AB}$  is the total energy of the complex,  $E_A$  is the subunit A's energy,  $E_B$  is the subunit B's energy, and  $E_{\text{int}}$  is the dissociation energy.<sup>12,13</sup>

Typically, several corrections have to be made to the above dissociation energy. These are the basis set superposition errors (BSSE)<sup>14</sup> and zero point energy corrections.<sup>15</sup> When calculating the complex energy, the basis set used for the complex is made up of all the basis sets used for the subunits. But the energy for a subunit is calculated with only its own basis set. It is necessary to include the B's basis functions when calculating  $E_A$  and vice versa for  $E_B$  calculation so that

the basis set used for AB, A and B are consistent. The discrepancy introduced without such basis set consideration is termed BSSE. Boys and Bernardi's counterpoise correction method has been used for BSSE.<sup>16</sup> It calculates the energy of the subunit with its own basis set and with the complex basis sets. Then simple subtractions and additions are made to generate the BSSE values, *CP*.

$$CP = E_A(A) + E_B(B) - E_A(AB) - E_B(AB) \quad (2.6)$$

Regarding the zero point energy correction, the harmonic calculations are first performed for all conformers. All the calculated frequencies are checked to make sure there are no imaginary frequencies. This allows one to determine whether a structure is at the saddle point of the potential energy surface or at a true minimum. From the harmonic calculations, the zero point energies of all the subunits and the complex are obtained. Again, simple subtraction and addition are used to give the zero point energy correction.

$$\Delta E_0 = E_{AB} - E_A - E_B \quad (2.7)$$

where  $\Delta E_0$  is the calculated zero point energy corrections,  $E_{AB}$  is the complex's zero point energy, and  $E_A$  and  $E_B$  are the subunits' zero point energies.

## 2.3 Experimental approaches

### 2.3.1 FTIR Module

The FTIR-VCD spectrometer used in this research work is from Bruker Instrument. The key part of the FTIR module is a Michelson Interferometer. An

U-shaped silicon carbide lamp served as the IR source in our spectrometer. In a much simplified schematic diagram, the light emitted first goes through a beam splitter and is split to 50% : 50% at each of the two directions to a fixed mirror and a movable mirror (see Figure 2.1). Then the two light beams reflected are recombined to generate interference pattern which is a function of differences in the lengths of the paths of the two beams. The signal frequency out of the interferometer is largely reduced to the audio range following the equation below.

$$f = \frac{2\mathcal{V}_M}{c} \mathcal{V} \quad (2.8)$$

Where  $f$  is the signal frequency at the detector,  $\mathcal{V}_M$  is the moving mirror's constant velocity and  $\mathcal{V}$  is the light frequency.

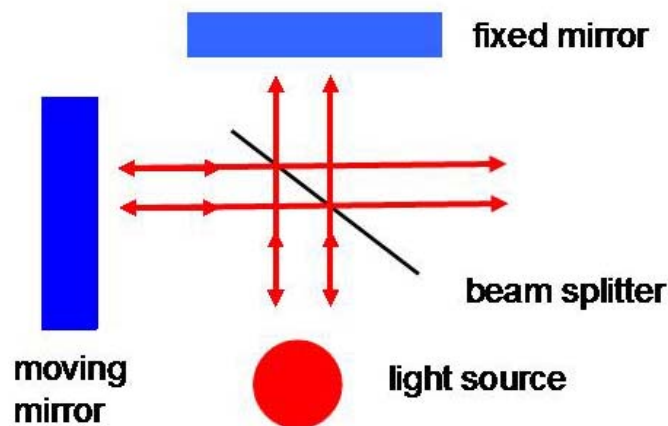


Figure 2.1: The simplified schematics of a general Michelson interferometer illuminated by a light source (figure reconstructed from ref 18) .

The typical mirror moving speed is 1.5cm/s, then  $f = 10^{-10} \mathcal{V}$ . Before the light beam reaches the detector, it first impinges on the sample which can be solid or liquid. A suitable sample holder is used based on the spectral range of interest. Both  $\text{CaF}_2$  and  $\text{BaF}_2$  have been used in my thesis work. The transmission curves of these two materials are shown in Figures 2.2 and 2.3.<sup>19</sup> In general,  $\text{BaF}_2$  is a better material in terms of its transmission curve. But this material is quite brittle and break fairly easily, compared to  $\text{CaF}_2$ .

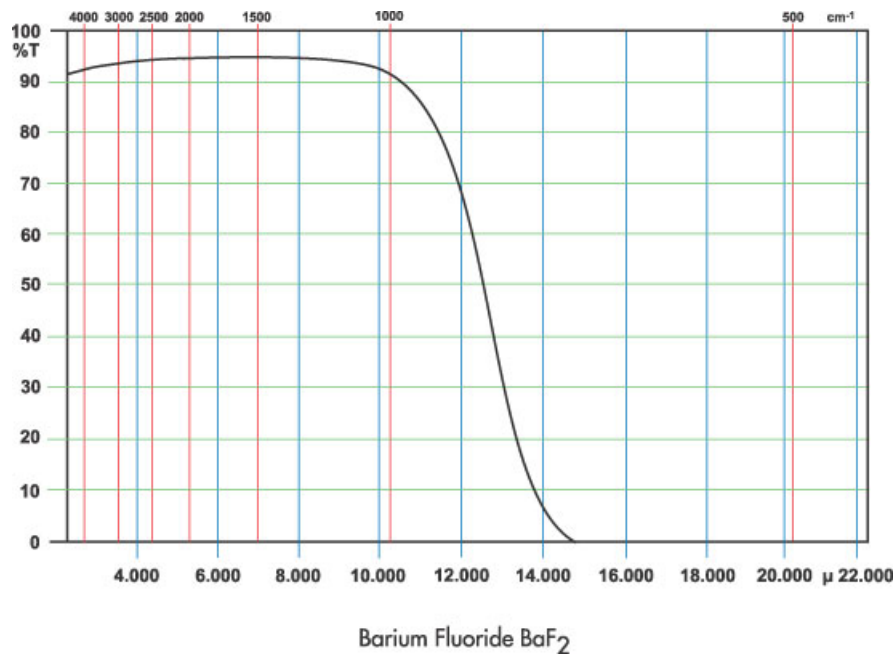


Figure 2.2: The transmission curve of  $\text{BaF}_2$  in the spectral range from 4000 to 500  $\text{cm}^{-1}$  (figure taken from ref 19).

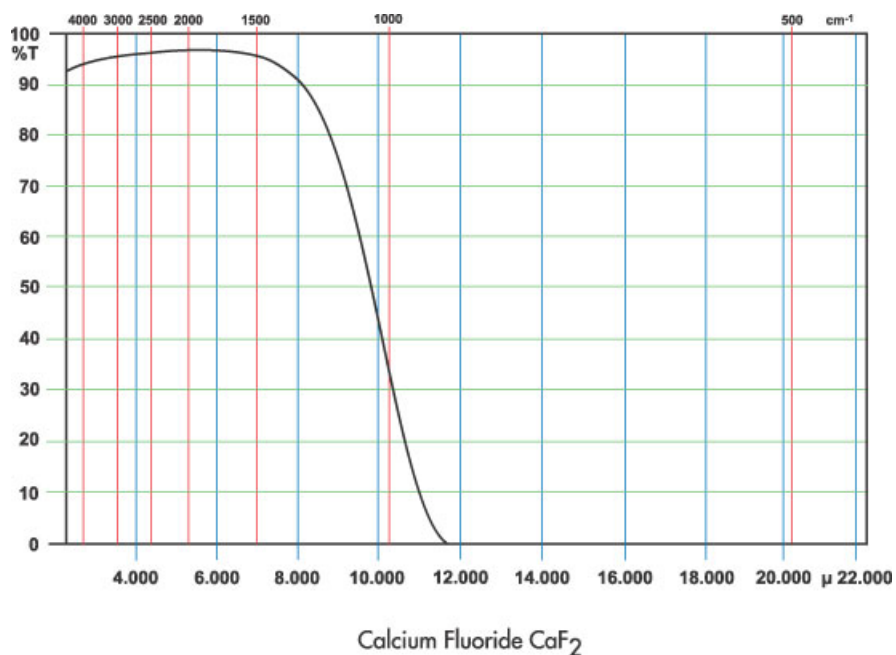


Figure 2.3: The transmission curve of CaF<sub>2</sub> at the spectral range from 4000 to 500 cm<sup>-1</sup> (figure taken from ref 19).

### 2.3.2 The VCD module<sup>20,21</sup>

The VCD module is attached to the FTIR module. It measures the differential absorptions between left and right circularly polarized light. The same light source from the interferometer is redirected to this VCD module. It then passes through a low-pass filter with a cut off at 1850 cm<sup>-1</sup>, a linear polarizer, a photoelastic modulator (PEM), the sample, and is finally focused onto a liquid nitrogen cooled Mercury Cadmium Tellurium (MCT) IR detector. The key optical component of the VCD device is the PEM. It is a bar made of ZnSe with an intrinsic resonant frequency at 50 kHz and is driven by an electronic driver which generates the

necessary voltage at such a modulation frequency. The light first goes through a filter where any frequency larger than  $1800\text{ cm}^{-1}$  is cut off. Then the light will go through a linear polarizer where the unpolarized light from the IR compartment becomes linearly polarized light. The polarizer is aligned so that the polarization direction reaches the PEM at  $45^\circ$  to the modulator axis. The polarized light can be decomposed into two orthogonal components. One with its electric vector parallel to the PEM axis and the other with its vector perpendicular to it. As the modulator stretches and compresses, the speed of the light at these two directions will be retarded accordingly. Specifically speaking, when it compresses, the parallel light experiences no retardation at all, whereas the perpendicular one does. On the contrary, when the modulator stretches, the perpendicular light is unaffected, whereas the parallel one is retarded. Therefore, the parallel light leads the perpendicular light when the modulator is compressed, whereas the perpendicular light leads the parallel light when the PEM stretches. If the phase difference is exactly 90 degree between the perpendicular and the parallel beams, the light after the PEM becomes right circularly polarized. If the phase difference is exactly 270 degree, then it becomes left circularly polarized light. These two cases are depicted in Figures 2,4 and 2,5. Otherwise, the light will become elliptically polarized light, except when the phase difference is 180 degree, then it becomes linearly polarized light with 90 degree rotation.

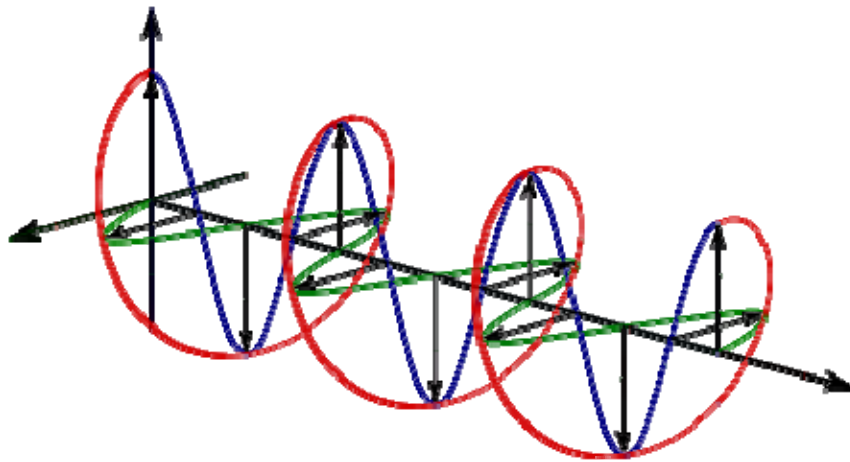


Figure 2.4: Right circularly polarized light generated by between the two linearly polarized lights (blue and green) with a 90 degree phase difference (figure taken from ref 22).

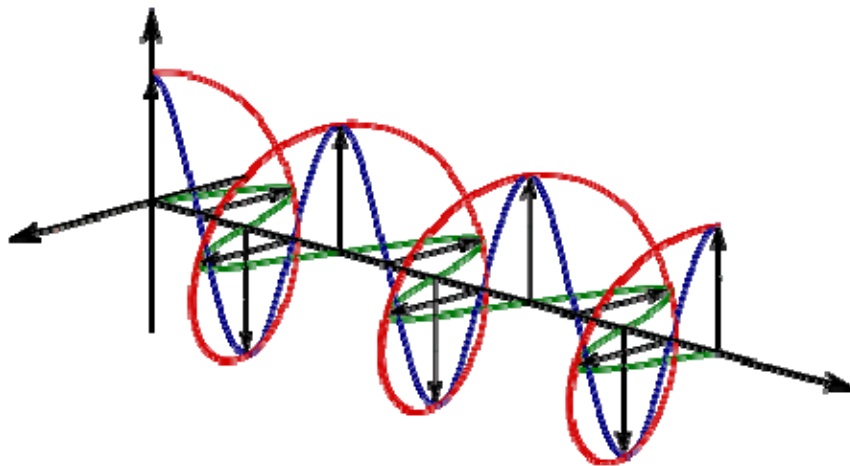


Figure 2.5: Left circularly polarized light generated by the two linearly polarized lights (blue and green) with a 270 degree phase difference (figure taken from ref 22).

After the light goes through the sample, it is collected at the MCT detector. The output signal from the detector is first amplified by a pre-amplifier. Then it goes through two different paths. The first path has a low-pass filter to filter the signal which is then processed to produce the IR spectrum, whereas the second path processes the signal with a lock-in amplifier. The signal is demodulated using a lock-in amplifier with its reference frequency being the modulation frequency of 50 kHz. This modulation scheme is essential since the VCD signal is about  $10^4$  to  $10^6$  times weaker than the corresponding IR signal. The demodulated interferogram originated from the interferometer is then FT from the centimeter domain to the wavenumber domain to give the spectrum. The instrumental set up is depicted in the figure 2.6.

## VCD spectrometer

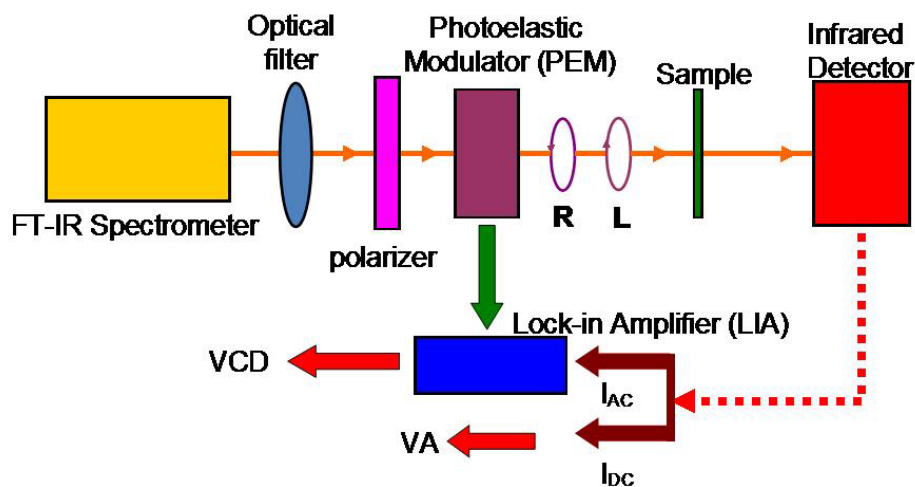


Figure 2.6: The general layout of FTIR-VCD spectrometer (figure is reconstructed from ref 23).

### 2.4 Matrix Isolation System

The matrix isolation system in our laboratory is from Advanced Research System. It consists of three main parts: a cryostat (or cold head), a helium closed recycle refrigerator, and a cold finger. It is layed out in the figure 2.7.

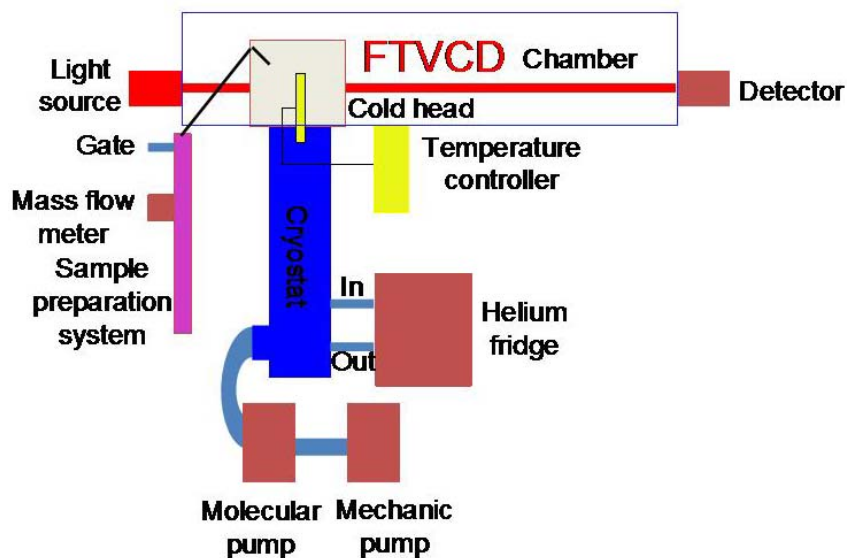


Figure 2.7: The schematics of a FT-VCD spectrometer coupled with a matrix isolation system.

The refrigerator can reach a temperature as low as 4K. An optical holder made of copper is attached to the cold finger and any gaps in between are filled with indium foil to ensure good thermal conductivity. The optics window is made of BaF<sub>2</sub>, where the desired sample is deposited. To reduce external radiation, which can lessen the cooling power of fridge, the cold head and the cold finger are shrouded with a highly reflective surface cover.

The whole apparatus except the refrigerator is maintained under high to ultrahigh vacuum when the system is in operation. A molecular pump from Pfeiffer Instruments backed by a regular mechanical pump is used for this purpose. We can maintain a vacuum condition as  $10^{-8}$  mbar after 2 days of pumping. Once

the system is under ultrahigh vacuum, the fridge can be turned on. The cryostat needs to be isolated by a shutter once the temperature gets lower than 35K. When finishing the experiment, the system needs to warm up to room temperature before breaking the isolation. Otherwise, condensation will build up inside the cryostat and it will take a long time to pump it clean again.

An ancillary system, consisting of a gaseous sample mixing and storing system and mass flow meters, is required before sample deposition. The flow rate is controlled by a MKS Instrument mass controller. It was calibrated using the N<sub>2</sub> gas as the standard one and some calibrations should be done for other molecules.

It is very critical to reach a stable temperature for a good MI experiment. The Lake Shore 311 model temperature controller is used for this purpose. It provides temperature readouts for the two silicon diode sensors installed and controls a heater. One can change the temperature according to the experiment purposes, such as performing an annealing procedure, through which the molecule can reach the local minimum energy structure. There are two silicon diode sensors used. One is mounted by the company to the cold head and the second one by us to the sample holder so that we know the temperature of the sample film more accurately. It is essential to properly anchor the sensor so that no heat leak is introduced. Once the matrix sample is ready, the optical head part can be inserted into the sample compartment of the IR or the VCD chambers for measurements.

## References:

- 1 Frisch, M. J.; Trucks, G. W.; Schlegel, H. B.; Scuseria, G. E.; Robb, M. A.; Cheeseman, J. R.; Montgomery, J. A.; Vreven, T.; Kudin, K. N.; Burant, J. C.; Millam, J. M.; Iyengar, S. S.; Tomasi, J.; Barone, V.; Mennucci, B.; Cossi, M.; Scalmani, G.; Rega, N.; Petersson, G. A.; Nakatsuji, H.; Hada, M.; Ehara, M.; Toyota, K.; Fukuda, R.; Hasegawa, J.; Ishida, M.; Nakajima, T.; Honda, Y.; Kitao, O.; Nakai, H.; Klene, M.; Li, X.; Knox, J. E.; Hratchian, H. P.; Cross, J. B.; Adamo, C.; Jaramillo, J.; Gomperts, R.; Stratmann, R. E.; Yazyev, O.; Austin, A. J.; Cammi, R.; Pomelli, C.; Ochterski, J. W.; Ayala, P. Y.; Morokuma, K.; Voth, G. A.; Salvador, P.; Dannenberg, J. J.; Zakrzewski, V. G.; Dapprich, S.; Daniels, A. D.; Strain, M. C.; Farkas, O.; Malick, D. K.; Rabuck, A. D.; Raghavachari, K.; Foresman, J. B.; Ortiz, J. V.; Cui, Q.; Baboul, A. G.; Clifford, S. Gaussian 03, Revision C.02, Gaussian, Inc.: Pittsburgh, **2003**
- 2 Bernath, P. F. *Spectra of Atoms and Molecules*, Oxford University Press: Oxford, **1995**.
- 3 Stephens, P. J.; Lowe, M. A. *Ann. Rev. Phys. Chem.*, **1985**, *36*, 214.
- 4 Stephens, P. J. *J. Phys. Chem.* **1985**, *89*, 748.
- 5 Honnenber, P. D.; Kohn, W. *Phys. Rev.* **1964**, *135*, B864.
- 6 Kohn, W.; Shan, L. *J. Phys. Rev.* **1965**, *140*, A1133.
- 7 Labanowski, J. K., Andzelm, J. W. *Density functional Methods in Chemistry*, Springer-Verlag: New York, **1991**.
- 8 Portmann, S.; Inauen, A.; Luthi, H. P.; Leutwyler, S. *J. Chem. Phys.* **2000**, *113*, 9577.
- 9 Krishnan, R.; Binkley, J. S.; Seeger, R.; Pople, J. A. *J. Chem. Phys.* **1980**, *72*, 650.
- 10 Becke, A. D. *J. Chem. Phys.* **1993**, *98*, 5648.
- 11 Lee, C. T.; Yang, W. T.; Parr, R. G. *Phys. Rev.* **1994**, *94*, 1873.
- 12 Hirschfelder, J. O.; Curtiss, C. F.; Bird, R. B. *Molecular Theory of Gases and Liquids*, Wiley: New York, **1964**, p. 921.
- 13 Szalewicz, K.; Jeziorski, B. *J. Chem. Phys.* **1998**, *109*, 1198.

- 14 Liu, B.; MeLean, A. D. *J. Chem. Phys.* **1973**, *59*, 4557.
- 15 Cramer, C. J. *Essentials of Computational Chemistry: Theories and Models*, 2<sup>nd</sup> edition, Wiley, **2002**.
- 16 Boys, S. F.; Bernardi, F. *Mol. Phys.* **1970**, *10*, 553.
- 17 Skoog, D. A.; Joller, F. J.; Couch, S. R. *Principles of Instrumental Analysis*, 6<sup>th</sup> edition, Tomson, **2007**. Chapter 16.
- 18 <http://elchem.kaist.ac.kr/vt/chem-ed/optics/selector/michelso.htm>
- 19 [http://www.internationalcrystal.net/optics\\_06.htm](http://www.internationalcrystal.net/optics_06.htm).
- 20 FT-IR/VCD Manuals from Bruker Optics
- 21 Wang, B. Application note from Hinds Instruments.
- 22 [http://en.wikipedia.org/wiki/Circular\\_polarization](http://en.wikipedia.org/wiki/Circular_polarization)
- 23 Freedman, T. B.; Cao, X.; Dukor, R. K.; Narie, L. A. *Chirality*, **2003**, *15*, 745.

# **Chapter 3\* Vibrational absorption, vibrational circular dichroism, and theoretical studies of methyl lactate self-aggregation and methyl lactate-methanol intermolecular interactions**

This chapter is directly copied from the published paper.<sup>1</sup> I have done all the ab initio calculations and experiments and written the first draft of the paper. The molecular dynamics calculations were performed by Dr. Guochun Yang. Dr. Martin Losada was involved in this project at the early stage and made helpful suggestions.

## **3.1 Introduction:**

It has long been recognized that intermolecular interactions between chiral solute molecules and between solute-solvent molecules can have profound and yet sometimes non-intuitive effects on the optical activity measurements.<sup>2</sup> To properly account for such effects is a long standing challenge in stereochemistry and in life science. For example, it was reported that the optical rotatory dispersion (ORD) spectrum of propylene oxide in the gas phase resembles more closely the corresponding spectrum in water, rather than in benzene.<sup>3</sup> In fact, the benzene

---

\* A version of this chapter has been published. Liu, Y.; Yang, G.; Losada, M.; Xu, Y. 2010, *The Journal of Chemical Physics*, 12:234513-234523

mediated specific optical rotation (OR) values are not only of very different magnitudes compared to the gas phase values but are of opposite signs.<sup>3</sup> The large negative ORD values obtained was attributed to imprint of chirality on benzene solvent by propylene oxide in a recent combined molecular dynamics (MD) and time-dependent density functional (DFT) study.<sup>4</sup> The positive OR value of propylene oxide in aqueous solution, on the other hand, was found to be dominated by the OR response of the propylene oxide-water binary complex, rather than propylene oxide itself.<sup>5</sup> This conclusion was further supported by the detailed experimental and ab initio studies of vibrational circular dichroism (VCD) and ORD spectroscopy of propylene oxide in water and by the gas phase rotational studies of the PO-(water)<sub>1,2</sub> clusters.<sup>6</sup> Because VA and VCD spectroscopic experiments are typically carried out for molecules in their ground electronic states, the corresponding theoretical simulations are considerably more reliable than, for example, the related ORD calculations. The combination of VA and VCD spectroscopy with DFT calculations and MD simulations, can therefore provide accurate and valuable information about the intermolecular interactions in solution<sup>7,8,9</sup> In particular, VCD spectroscopy shows high sensitivity to conformational changes and is well suited as a spectroscopic tool to probe intermolecular interactions<sup>10</sup> in solution or in matrix<sup>11</sup>.

In this study, we are interested in the intermolecular hydrogen (H)-bonding

interactions of methyl lactate (ML) in the methanol and carbon tetrachloride solutions. ML is the simplest member of the lactate ester group. It contains several important functional groups and has a relatively small number of atoms and electrons, making it suitable for high level *ab initio* calculations. Because of these desirable properties, ML and ML containing complexes had been studied extensively before. For example, its H-bonded complexes were used as prototypes for modelling chiral molecular recognition interactions in the gas phase.<sup>12,13</sup> The ML monomer exists in several different conformations.<sup>14,15</sup> The lowest energy monomeric conformer (Figure 3.1) contains an intramolecular OH $\cdots$ O=C H-bond and accounts for over 90% of the total population. Its ground state rotational spectrum was recorded where hyperfine structures due to the internal rotations of the two methyl internal rotators were detected and analyzed.<sup>14</sup>

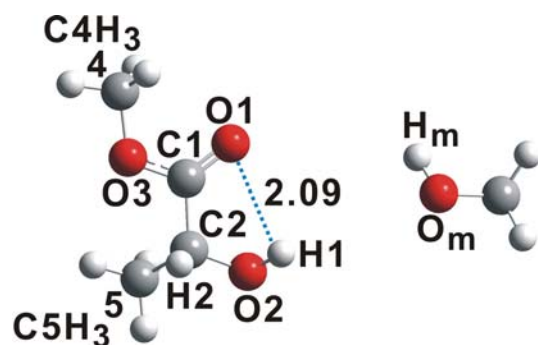


Figure 3.1. Atom labelling for both ML and methanol. The dominant conformer of ML which has ~90% of the monomer population is shown.

Several higher energy conformers were identified in a matrix isolation vibrational spectroscopic study.<sup>15</sup> The intermolecular interaction between ML and methanol is also of great interest in light of the fact that lactate esters have emerged in recent years as environmentally friendly solvents in industry to replace the hazardous and polluting organic solvents because of its non-toxicity and steady biodegradability.<sup>16</sup> For this reason, the ML and ethyl lactate liquids and their methanol solutions were subjects of several recent theoretical studies.<sup>17</sup> In addition, the intermolecular interactions between ML and water in the solution phase were very recently investigated using VA and VCD spectroscopy together with DFT calculations. The evidence of chirality transfer, i.e., some vibrational bands of the achiral water subunits gain substantial VCD strength upon complexation with a chiral ML molecule, was reported.<sup>18</sup> In this report, we focus on analyzing the effects of the intermolecular H-bonding interactions on the VA and VCD spectra of ML in methanol and in carbon tetrachloride using MD simulations and ab initio calculations. We aim to provide quantitative understanding of the dominant explicit intermolecular interactions in solution.

### **3.2 Experimental**

Both (*S*)-ML and (*R*)-ML (Acros Organics) were used without further purification. For solution preparation, methanol of spectrophotometric grade ( $\cong$  99.9 %, Sigma-Aldrich) was used. The VCD spectra were obtained using a

Fourier transform (FT) infrared spectrometer (Vertex 70, Bruker) equipped with a VCD module (PMA 50, Bruker). The details of the experimental set up had been described before.<sup>18</sup> Briefly, a low pass filter with a cutoff wavenumber  $1800\text{ cm}^{-1}$ , a linear polarizer, and a 50 kHz ZnSe photoelastic modulator were used. The absorption signals were detected using a liquid nitrogen cooled MCT infrared detector with a  $\text{BaF}_2$  window. The signals were then demodulated using a lock-in amplifier (Stanford Research Systems 830). A spectral resolution of  $4\text{ cm}^{-1}$  was used for both VA and VCD measurements. The liquid samples were placed in a demountable cell (International Crystal) with  $\text{CaF}_2$  windows. Different sets of concentrations and path lengths had been tried. Because of the strong VA absorption of ML at  $\sim 1746\text{ cm}^{-1}$  and the medium strong one of methanol from  $1350\text{ cm}^{-1}$  to  $1450\text{ cm}^{-1}$ , it is necessary to use a very short path length. The experimental spectra reported were measured by placing the 2.0 M ML in methanol and in  $\text{CCl}_4$  between two  $\text{CaF}_2$  plates without a spacer. The path length was estimated to be  $\sim 6\text{ }\mu\text{m}$ , although small variations were noticed, depending how tightly one secured the screws. The corresponding solvent spectra obtained under identical conditions were subtracted off in the VA spectra. For the VCD spectra shown, the racemic spectra were subtracted from the enantiopure spectra. This was performed to minimize any artefacts that are not due to chirality since VCD signals are generally about  $10^4$  to  $10^6$  times weaker than the corresponding VA signals and are more susceptible to artefacts. The VA and VCD spectra of 0.2

M ML in  $\text{CCl}_4$  was obtained with a path length of 100  $\mu\text{m}$  in a previous study.<sup>18</sup>

### 3.3 Computational Methods

#### 3.3.1 MD simulation

MD simulations were carried out using the Sander module in the AMBER9 suite of programs.<sup>18</sup> Three simulations were performed for a box with 21 ML molecules and 209 methanol molecules, and a box with 21 ML and 86  $\text{CCl}_4$ . These correspond to the experimental conditions used in the present study: 2 M ML in methanol and 2M ML in  $\text{CCl}_4$ . The AMBER *ff99* force field<sup>19</sup> based on molecular mechanics was used in the simulation. To remove bad contacts, the initial configuration was first relaxed by applying 500 steps of steepest descent algorithm, followed by 500 steps of conjugate gradient algorithm. The final configuration thus obtained was used as the starting point for a MD simulation under *NVT* condition. In the simulation, the system was first heated from 0 to 298 K in 100 ps, followed by a 300 ps equilibrating period to ensure that the equilibrium was reached completely. A 7 ns production MD simulation was then performed under *NPT* condition ( $T=298$  K,  $P=1$  atm). The particle mesh Ewald summation method<sup>20,21</sup> was used to treat the long-range electrostatic interactions and the SHAKE algorithm<sup>22</sup> was used to constrain all H-atom containing covalent bonds. A 7 Å cutoff was set for the noncovalent interactions. The MD simulation time step was 2 fs.

### 3.3.2 *ab initio* calculations

The *ab initio* calculations were performed using Gaussian 3.0 package.<sup>23</sup> The geometry optimizations, the harmonic frequency calculations, the VA and VCD intensity calculations were performed using the 6-311++G\*\* basis sets with density functional theory (DFT). (R)-ML is used in all simulations in this paper unless specified otherwise. The functional used in all is the Becke's exchange and Lee, Yang, and Parr's functional (B3LYP).<sup>24</sup> The basis sets and the functional were chosen because they are well suited to describe the intermolecular H-bonding and have been used in a number of related studies.<sup>6-12,18</sup> The snap shots generated in the MD simulations were used to identify the possible clusters in solution. The initial geometry searches for the possible conformers of ML-(methanol)<sub>1,2,3</sub> were performed with a smaller basis set 6-31+G\*. The final geometries for all clusters were carried out using the 6-311++G\*\* basis set. The geometries were fully optimized without any symmetry restrictions. The most stringent convergence criteria (e.g. gradient norm < 10<sup>-6</sup>) were used in all cases. The raw dissociation energies were corrected for the zero point energy (ZPE) effect and for the basis set superposition errors (BSSE) using the full counterpoise procedure.<sup>25,26</sup> The reported DFT harmonic frequencies were uniformly scaled with an empirical scaling factor of 0.98 when comparing with the experimental data. To obtain more reliable relative energies, single point MP2/6-311++G\*\* calculations at the DFT optimized geometries were also performed for the relevant conformers of

ML-(methanol)<sub>1,2,3</sub>.

### **3.4 Results and Discussions**

#### **3.4.1 Experimental VA and VCD spectra of ML in methanol and in carbon tetrachloride**

The experimental VA and VCD spectra of 2 M ML in methanol and in CCl<sub>4</sub> are given in Figure 3.1, together with the corresponding spectra of 0.2 M ML<sup>18</sup> in CCl<sub>4</sub> for comparison. The VCD spectra of the 2 M methanol and CCl<sub>4</sub> solutions of both enantiomers, showing basically mirror images to each other, are also provided in Figure 3.1.

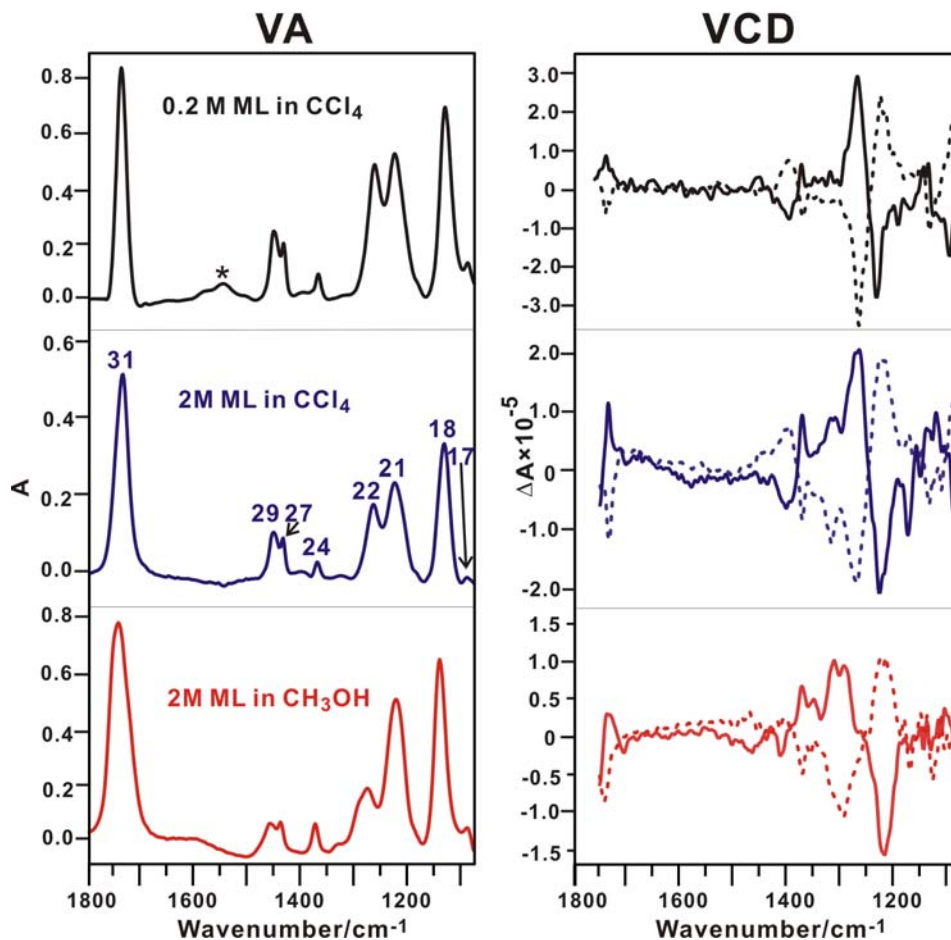


Figure 3.2 The experimental VA and VCD spectra of 0.2 M and 2M ML in  $\text{CCl}_4$  and 2M ML in methanol. The solid line (—) in the VCD spectra is for (*R*)-ML while the dotted line (---) is for (*S*)-ML.

The center wavenumbers and the assignment of the visible VA peaks are listed in Table 1. It had been shown, in a recent publication, that the VA and VCD spectra of the 0.2 M ML in  $\text{CCl}_4$  could be well modeled by considering only the

monomeric ML conformers.<sup>18</sup> The most obvious visual change in the VA spectrum, going from 0.2 M to 2 M in CCl<sub>4</sub>, is the intensity ratio of the two closely spaced peaks, labeled as 22 and 21. While they are about the same relative intensity in the 0.2 M solution, peak 21 becomes noticeably stronger relative to peak 22 in the 2 M solution. Other changes include the slight broadening of peak 31 at ~1741 cm<sup>-1</sup> and of peaks 21.

Table 3.1 Observed fundamental VA bands for ML in the CCl<sub>4</sub>, methanol and water solvents. All frequencies are in cm<sup>-1</sup>.

Approximate Assignment <sup>a</sup>	Band	0.2 M in CCl <sub>4</sub> <sup>c</sup>	2M in CCl <sub>4</sub>	2M in MeOH	2M in water <sup>c</sup>
$\nu(\text{C1}=\text{O1})$	31	1741	1741	1746	1733
$\delta(\text{C4H}_3)_{as'} + \delta(\text{C5H}_3)_{as'}$	29	1454	1455	1458	1456
$\delta(\text{C4H}_3)_{as''}$	27	1438	1438	1439	1441
$\delta(\text{C5H}_3)_s$	24	1373	1373	1374	1378
$\delta(\text{C2-O2-H1}) + \nu(\text{C1-O3})$	22	1265	1267	1275	1293
$\nu(\text{C1-O3}) + \tau(\text{C2-H2})$	21	1228	1226	1221	1236
$\nu(\text{C2-O2}) + \gamma(\text{C4H}_3)'$	18	1133	1133	1139	1133
$\nu(\text{C2-C5H}_3)$	17	1090	1091	1091	1085

<sup>a</sup> See Figure 3. 1 for the atom labelling.  $\nu$ , bond stretching,  $\delta$ , bending,  $\gamma$  rocking, and  $\tau$ , torsion.

<sup>b</sup> Band numbering is based on the calculated harmonic fundamentals. *s* indicates symmetric bending and *as* asymmetric bending.

<sup>c</sup> Ref. **Error! Bookmark not defined.**

From Table 1, one can see that peak 31 which corresponds mainly to the C=O stretching experiences no observable shift, while the two closely spaced peaks 22 and 21 are slightly blue and red shifted by  $\sim 2\text{cm}^{-1}$ , respectively. All these structures indicate the existence of intermolecular H-bonding interactions of ML in the 2 M solution, most likely due to the self-aggregation of the ML molecules. Some changes were also noted in the related VCD spectra, for example, a new peak appears at  $\sim 1315\text{ cm}^{-1}$ . Somewhat similar but much more profound changes, in both the VA and VCD spectra of the 2M ML in methanol, have been observed. For example, peak 31 is now severely broadened. The relative intensity ratio of peak 21 vs 22 increases to about 3:1 from the  $\sim 1:1$  ratio in 0.2M  $\text{CCl}_4$  and peak 22 and 21 experience again blue and red shift but in the larger amount of 10 and  $7\text{ cm}^{-1}$ , respectively. From Table 1, one can see that the general trend of the blue and red shift of peaks is the same for 2M ML in methanol and in water with two noticeable exceptions. First, peak 31 which is related to the C=O stretching is blue shifted by  $5\text{ cm}^{-1}$  in methanol, in contrast to a red shift of  $8\text{ cm}^{-1}$  in water. Second, peak 21 experiences a red shift of  $7\text{ cm}^{-1}$  and a blue shift of  $8\text{ cm}^{-1}$  in methanol and in water, respectively. One can expect that these changes in

methanol are caused by the intermolecular interactions between ML and methanol and by perhaps of the ML self-aggregation to some degree. Some differences observed with methanol and water, are likely related to the more subtle dissimilarity of how these two solvent molecules interact with ML. In addition, the different dielectric environments provided by CCl<sub>4</sub> and methanol may also play a role in the different appearance of the observed spectra in these two solvents. In the following, we utilize MD and ab initio theoretical investigations to analyze and to understand the above observations at a microscopic molecular level.

### **3.4.2 Simulations of the VA and VCD spectra of ML in methanol and CCl<sub>4</sub>**

It is clear that the experimental observed differences in the VA and VCD spectra of the 0.2 M and 2 M ML in CCl<sub>4</sub> solution can not be explained using an implicit polarizable continuum model (IPCM)<sup>27</sup> since the solvent in both cases is the same. Nevertheless, we had simulated both VA and VCD spectra of ML in methanol with IPCM and compared them with those obtained for the gas phase ML monomer and for the ML in CCl<sub>4</sub> in Figure S1 (available as supporting information). As one can see, inclusion of the IPCM solvents cannot explain the major differences observed experimentally for these three different experimental conditions. Rather, the explicit H-bonding interactions between solvent-solute and solute-solute molecules have to be taken into account.<sup>6,8,9,18</sup> In the following, we

describe the theoretical modelling carried out for our targeted molecular systems.

### **3.4.2.1 Coordination number of the first methanol shell and the degree of ML self-aggregation in methanol**

MD simulations had been used in a number of recent studies to provide useful information about the short-range H-bonding structures and dynamics in solution on a microscopic level<sup>5,8,9,29</sup> In order to estimate, for example, the number of methanol molecules explicitly H-bonded to a ML molecule in solution and to survey the geometries of a large number of possible small ML-(methanol)<sub>N</sub> clusters, MD simulations were carried out in this study. Information about these H-bonding structures can be obtained from the analyses of atom-atom radial distribution functions (RDFs). A RDF,  $g(r)$ , characterizes the average density of certain particles at a distance  $r$  from an arbitrarily defined central atom. ML has three functional groups, and the three oxygen atoms of which are labelled as O1, O2, and O3 (see Figure 3.1 for atom labelling). These functional groups can form intermolecular H-bonds with methanol. The RDFs of the O<sub>m</sub> and H<sub>m</sub> of the methanol molecules around O1, O2, and O3 of a ML molecule, denoted as  $g(r)_{O1H_m}$ ,  $g(r)_{O2H_m}$ ,  $g(r)_{O3H_m}$  and  $g(r)_{O1O_m}$ ,  $g(r)_{O2O_m}$ , and  $g(r)_{O3O_m}$  respectively, are presented in Figure 3.3.

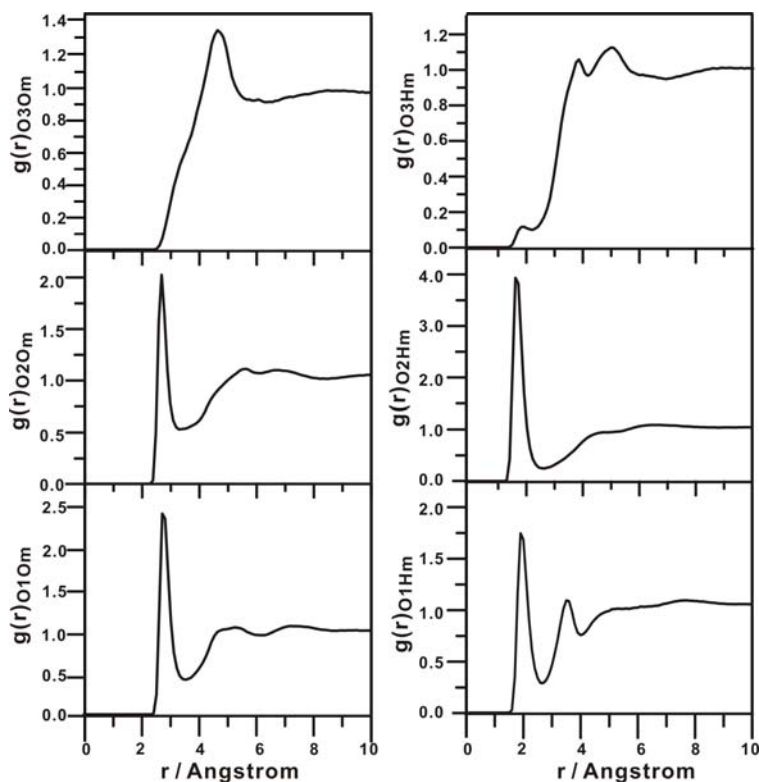


Figure 3.3 RDFs obtained from the MD simulation of 2M ML in methanol. The RDFs shown are related to the intermolecular interactions between ML and methanol. See Figure 3.1 for atom labelling of ML and methanol.

The  $g(r)_{O1Hm}$  and  $g(r)_{O2Hm}$  functions, each reaches its first maximum at 1.75 Å and the next minimum at 2.55 Å, while the first maxima of  $g(r)_{O1Om}$  and  $g(r)_{O2Om}$  appear at  $\sim 2.85$  Å and the next minima at 3.55 Å. The well defined first peaks in these RDFs clearly indicate the H-bonding nature of the intermolecular interactions between O1 and Hm and O2 and Hm. While the first maximum of  $g(r)_{O3Om}$  and  $g(r)_{O3Hm}$  appears at  $\sim 4.55$  Å and 3.95 Å, respectively, which are

much larger than a typical intermolecular H-bonding distance. These maxima also have a much broader profile than those associated with O1 and O2. This indicates that the possibility of forming H-bonding between OH of methanol with O3 of ML is relatively low, comparing to at the sites of O1 or O2 of ML. Integration of the first peak out to the minimum in the above mentioned  $g(r)_{O1O_m}$  and  $g(r)_{O2O_m}$  functions gives a methanol coordination number of 1.53 and 1.23, respectively. From the above analyses, we conclude that the coordination number of the first methanol shell is about 3.

From the same MD simulation, one can obtain information about the self-aggregation of ML in methanol at 2.0 M concentration. To do that, we scanned the probability of finding the second ML molecule at the vicinity of the three functional groups, representing by O1, O2 and O3 atoms. The RDFs,  $g(r)_{O1O1}$ ,  $g(r)_{O1O2}$ ,  $g(r)_{O1O3}$ ,  $g(r)_{O2O2}$ ,  $g(r)_{O2O3}$ , and  $g(r)_{O3O3}$  are shown in Figure 3.4.

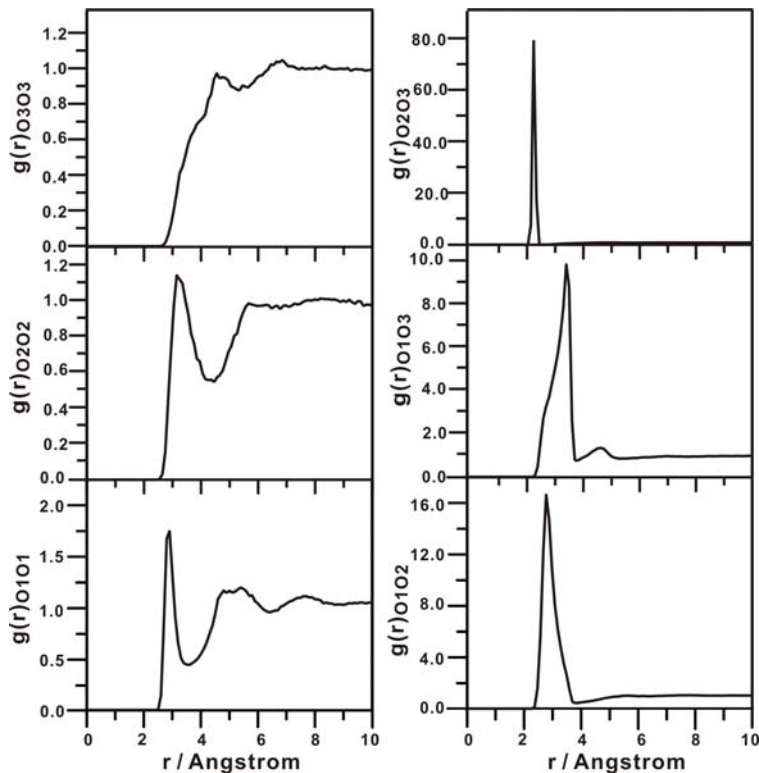


Figure 3.4 RDFs obtained from the MD simulation of 2M ML in methanol. The RDFs shown are related to the self-aggregation of ML in methanol. See Figure 3.1 for atom labelling of ML and methanol.

Both  $g(r)_{O1O1}$  and  $g(r)_{O2O2}$  have well defined sharp peaks with the first maximum at 2.85 Å and 3.05 Å, and the next minimum at 3.55 Å and 4.25 Å, respectively. The sharpness of the peaks suggests the nature of H-bonding interactions at the sites of O1 and O2. However, the integration of the first peak out to the minimum mentioned above in  $g(r)_{O1O1}$  and  $g(r)_{O2O2}$  gives a coordination number of 0.23 and 0.16, respectively. This indicates that the ML self-aggregation

with H-bonding at these two sites is not a dominant event in the present solution.  $g(r)_{O3O3}$  has a very broad features, suggesting there is little H-bonding character of the interactions at the site of O3. In addition, the first maximum peak of  $g(r)_{O1O2}$ ,  $g(r)_{O1O3}$ , and  $g(r)_{O2O3}$  appears at the corresponding the bond distance of O1–O2, O1–O3, and O2–O3 in the same ML molecule, respectively. From the above analyses, one can conclude that the ML self-aggregation is not a dominant event at the current experimental condition in methanol. Subsequently, we simulated the explicit intermolecular H-bonding interactions of ML in methanol solution using the small ML-(methanol) $_N$  clusters with  $N = 1,2,3$ .

#### **3.4.2.2 Dimer or larger self-aggregation ML clusters in CCl<sub>4</sub> ?**

ML has three functional groups and is capable of forming dimer or larger aggregation in CCl<sub>4</sub>. To obtain some information about the extent of the ML self-aggregation in CCl<sub>4</sub>, a MD simulation was performed for a box of 21 ML molecules and 86 CCl<sub>4</sub> molecules, which corresponds to the concentration of 2.0 M. We examined the six RDFs, i.e.  $g(r)_{O1O1}$ ,  $g(r)_{O1O2}$ ,  $g(r)_{O1O3}$ ,  $g(r)_{O2O2}$ ,  $g(r)_{O2O3}$ , and  $g(r)_{O3O3}$  (Figure 3.5), as we did previously for the self-aggregation of ML in methanol.  $g(r)_{O1O1}$  has two sharp peaks.

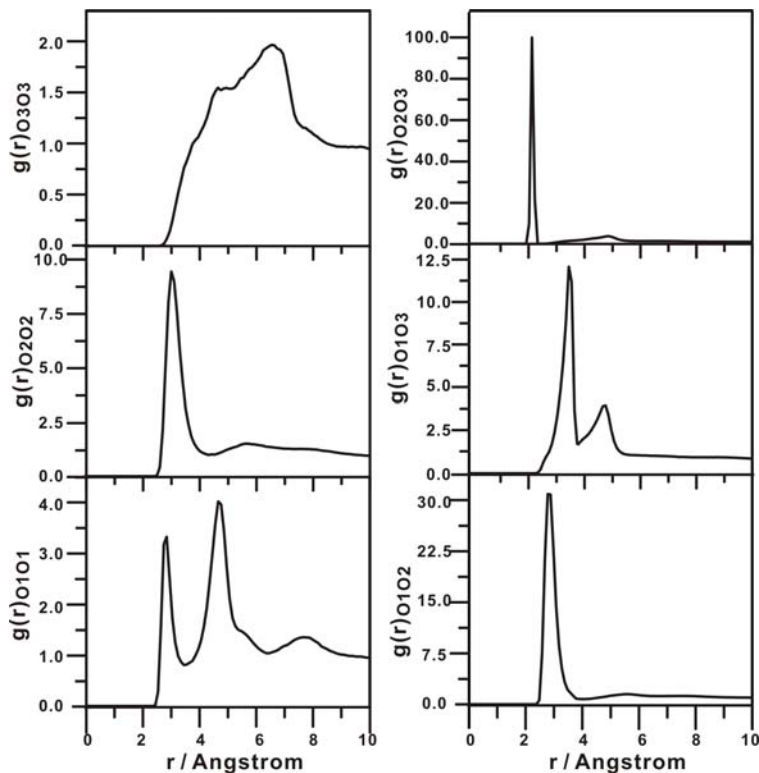


Figure 3.5 RDFs obtained from the MD simulation of 2M ML in  $\text{CCl}_4$ . The RDFs shown are related to the self-aggregation of ML in  $\text{CCl}_4$ . See Figure 3.1 for atom labelling of ML.

The first one at  $2.85 \text{ \AA}$ , corresponds to a  $\text{O1-H}\cdots\text{O1}$  type intermolecular H-bond. But the integration to the first minimum gives a value of 0.22, suggesting that such H-bonding is not a dominating event. The second peak at  $4.65 \text{ \AA}$ , corresponds to the *insertion* type intermolecular H-bond pattern mentioned above. The integration to the second minimum  $6.25 \text{ \AA}$  gives a value of 1.28.  $g(r)_{\text{O2O2}}$  has a well defined sharp peak at  $3.05 \text{ \AA}$  and reaches the next minimum at  $4.35 \text{ \AA}$ . The

integration to the first minimum is 1.07, corresponding to an *insertion* type intermolecular H-bond pattern where each ML opens up their intramolecular H-bonds simultaneously to form a larger intermolecular H-bonding ring (vide infra).  $g(r)_{O3O3}$  has no sharp features, indicating no H-bonding at the site of O3. The one prominent peak in  $g(r)_{O1O2}$ ,  $g(r)_{O1O3}$ , and  $g(r)_{O2O3}$  again appear at the corresponding the bond distance of O1–O2, O1–O3, and O2–O3 in the same ML molecule, respectively. This was also observed before in the case of ML in methanol. Based on the above discussion, we infer that ML may exist as monomer or dimer at 2.0 M concentration in  $CCl_4$  and the possibility of larger aggregation is very small. We therefore simulated the self-aggregation of ML in  $CCl_4$  using the ML dimers.

### 3.4.2.3 The 1:1, 1:2, and 1:3 ML-methanol clusters and the ML dimers

Since the most stable ML monomeric conformer (Figure 3.1) accounts for ~90% of the population, it was used to construct the ML-methanol clusters of interest. Methanol can attach to ML in two major ways, based on the previous ML-water study<sup>18</sup> and the snap shots generated in the MD simulations. First, the hydroxyl group of methanol can be inserted into the existing intramolecular H-bond between the carbonyl group and hydroxyl group of ML to form the *insertion* type conformers. Here both ML and methanol act simultaneously as H-bond donor and acceptor. Second, instead of breaking into the intramolecular

H-bond ring of ML, the hydroxyl group of methanol can be attached to each of the three oxygen atoms of ML to form the *addition* type conformers. One can in principle have a third scenario when ML acts only as H-bond donor and methanol only as acceptor to form  $O_2H_1 \cdots O_m$  bond. It can be expected that this type of conformers is much higher in energy, by simply counting the total number of the intra- and intermolecular H-bonds and comparing the number to those in the first two classes discussed above. This third class is therefore not included in our further discussions. In each of the above classes, one also needs to consider the relative orientations of the two unpaired electrons of each H-bonding oxygen atom. This may result in more possible conformers. All together, seven binary conformers were identified in the geometry optimizations were subsequently confirmed to be local minima by the corresponding harmonic frequency calculations. The geometries of the seven most stable conformers are given in Figure 3.6. The raw and the BSSE and ZPE corrected dissociation energies of these conformers, as well as their room temperature Boltzmann factors are given in Table 2. To further improve the reliability of the relative energies, single point MP2 energy calculations were also performed and the results are also summarized in Table 2.

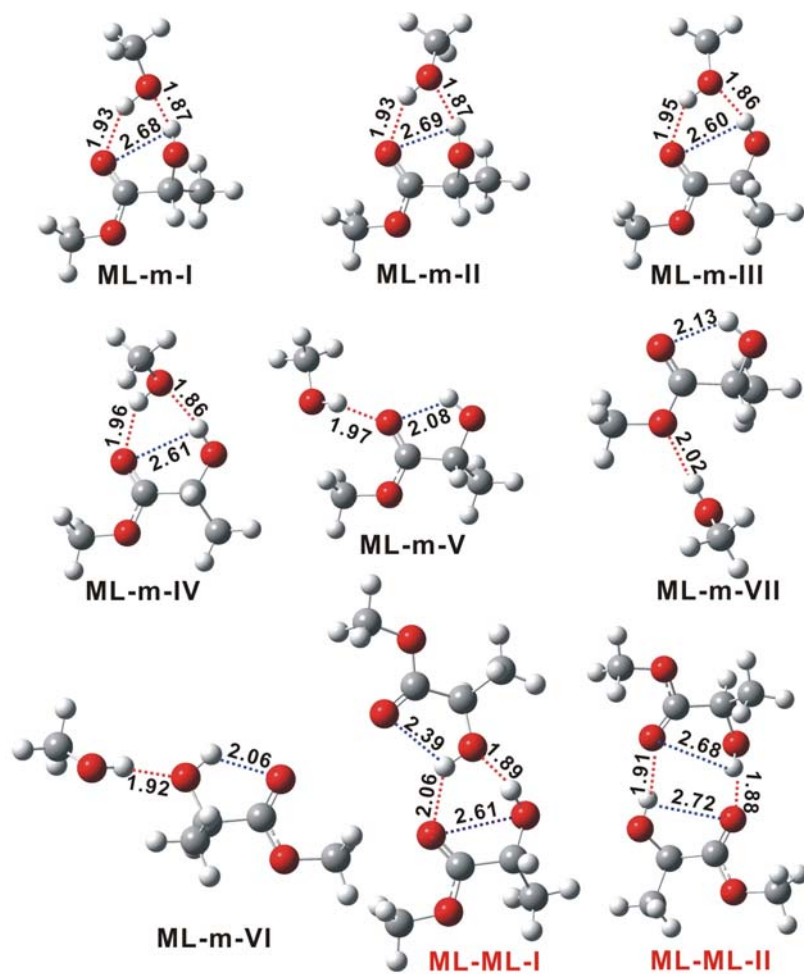


Figure 3.6 Optimized geometries of the seven most stable 1:1 ML-methanol conformers and the two ML dimers. The intermolecular and intramolecular hydrogen bond lengths are in the unit of Å.

Table 3.2 The raw dissociation energies ( $De$ ), the BSSE and ZPE corrections, the corrected dissociation energies ( $Do$ ), and the relative dissociation energies ( $\Delta Do$ ) of ML monomers and ML-methanol complexes at the B3LYP/6-311++G\*\* and the MP2/6-311++G\*\* level of theory. All energy values are in kcal mol<sup>-1</sup>.

Names	$De$	BSSE	$\Delta ZPE^b$	$Do^c$	$\Delta Do$	$b_f^d$
<b>ML-m-I</b>	-7.943 (-9.421) <sup>a</sup>	0.832 (0.884)	1.898	-5.214 (-6.638)	0.000 (0.000)	0.464 (0.553)
<b>ML-m-II</b>	-7.148 (-8.617)	0.793 (0.843)	1.754	-4.601 (-6.020)	0.613 (0.622)	0.167 (0.197)
<b>ML-m-III</b>	-7.309 (-8.496)	0.808 (0.865)	1.767	-4.735 (-5.864)	0.479 (0.769)	0.209 (0.152)
<b>ML-m-IV</b>	-6.588 (-7.740)	0.805 (0.846)	1.633	-4.150 (-5.262)	1.064 (1.388)	0.079 (0.056)
<b>ML-m-V</b>	-5.743 (-6.838)	0.631 (0.677)	1.301	-3.811 (-4.860)	1.403 (1.786)	0.045 (0.029)
<b>ML-m-VI</b>	-5.237 (-6.012)	0.467 (0.560)	1.087	-3.683 (-4.365)	1.531 (2.233)	0.036 (0.013)
<b>ML-m-VII</b>	-2.749 (-2.888)	0.605 (0.661)	0.661	-1.483 (-1.565)	3.731 (5.609)	0.001 (0.000)
<b>ML-2m-I</b>	-17.413 (-20.663)	1.935 (2.012)	3.325	-12.154 (-15.327)	0.000 (0.000)	0.254 (0.324)
<b>ML-2m-II</b>	-17.383 (-20.526)	1.952 (1.992)	3.419	-12.012 (-15.114)	0.142 (0.212)	0.201 (0.228)
<b>ML-2m-III</b>	-17.395 (-20.399)	1.974 (1.994)	3.475	-11.946 (-14.930)	0.208 (0.396)	0.180 (0.168)
<b>ML-2m-IV</b>	-17.035 (-20.049)	1.899 (1.977)	3.338	-11.799 (-14.735)	0.355 (0.592)	0.141 (0.121)
<b>ML-2m-V</b>	-17.218(- 20.066)	1.944 (1.988)	3.353	-11.921 (-14.725)	0.233 (0.602)	0.172 (0.119)

<b>ML-2m-VI</b>	-16.066 (-18.905)	1.857 (1.932)	3.144	-11.064 (-13.828)	1.090 (1.498)	0.041 (0.027)
<b>ML-3m-I</b>	-28.209 (-33.628)	3.210 (3.247)	4.946	-20.052 (-25.435)	0.000 (0.000)	0.513 (0.308)
<b>ML-3m-II</b>	-27.070 (-33.686)	3.211 (3.238)	5.108	-18.751 (-25.340)	1.301 (0.095)	0.059 (0.263)
<b>ML-3m-III</b>	-27.610 (-33.209)	3.093 (3.132)	4.920	-19.597 (-25.158)	0.455 (0.277)	0.240 (0.194)
<b>ML-3m-IV</b>	-26.616 (-33.364)	3.236 (3.265)	5.085	-18.295 (-25.015)	1.758 (0.420)	0.027 (0.153)
<b>ML-3m-V</b>	-26.493 (-32.052)	3.099 (3.131)	4.835	-18.559 (-24.086)	1.493 (1.349)	0.043 (0.033)
<b>ML-3m-VI</b>	-26.054 (-31.934)	3.167 (3.194)	4.888	-17.999 (-23.852)	2.053 (1.583)	0.017 (0.022)
<b>ML-3m-VI I</b>	-26.667 (-31.524)	3.081 (3.112)	4.726	-18.860 (-23.686)	1.192 (1.749)	0.070 (0.017)
<b>ML-3m-VI II</b>	-26.280 (-31.276)	3.070 (3.063)	4.826	-18.384 (-23.387)	1.669 (2.048)	4.888 (0.010)
<b>ML-ML-I</b>	-5.948 (-8.908)	0.861 (1.006)	1.363	-3.724 (-6.539)	0.000 (0.000)	0.699 (0.770)
<b>ML-ML-II</b>	-5.344 (-8.320)	0.764 (1.138)	1.363	-3.218 (-5.819)	0.507 (0.720)	0.301 (0.230)

<sup>a</sup> The corresponding single point MP2 energy values are given in parentheses.

<sup>b</sup>  $\Delta ZPE = ZPE(\text{complex}) - ZPE(\text{ML}) - ZPE(\text{methanol})$ .

<sup>c</sup>  $Do = De + BSSE + \Delta ZPE$ .

<sup>d</sup> The normalized Boltzmann factor at 298 K.

In generally, only relatively small changes in the relative energies of these binary conformers are noted going from the DFT to the MP2 energies. The 1:1 ML-methanol conformers are labeled with the names **ML-m-I**, **II**, and so on, where the capitals Roman letters indicate their relative stability based on their single point MP2 energies in Table 2. The six most stable geometries found are qualitatively the same as those identified before using MP2/6-31+G\*.<sup>12d</sup> The *additional* conformers, i.e. **ML-m-V**, **VI**, and **VII**, were found to be much less stable than the *insertion* conformers, **ML-m-I**, **II**, **III** and **IV**. In general, the H-bonding acceptor ability decreases going from the hydroxyl, the carbonyl, to the ester oxygen atoms. Similar finding was reported previously.<sup>18</sup>

For the larger ML-(methanol)<sub>2</sub> complex, we used the most stable *insertion* 1:1 conformers as starting points. Applying the same principle as describing above, we identified six most important the 1:2 ML-(methanol)<sub>2</sub> conformers. Although conformers with both *insertion* and *additional* H-bonds were also identified, those with only *additional* H-bonds are considerably less stable than the *insertion* ring geometries shown in Figure 3.7 and are therefore not shown.

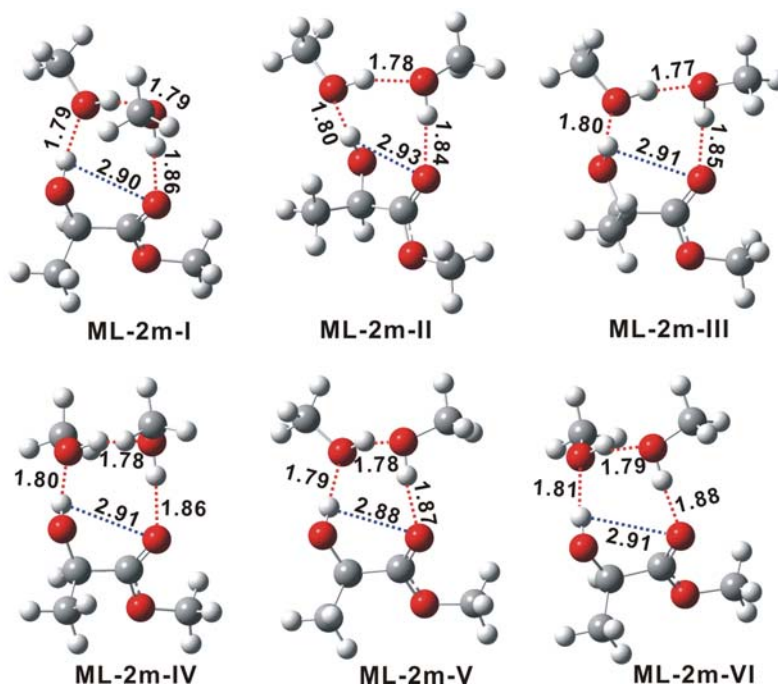


Figure 3.7 Optimized geometries of the six most stable 1:2 ML-methanol conformers. The intermolecular and the (secondary) intramolecular hydrogen bond lengths are in the unit of Å.

The corresponding raw and the BSSE and ZPE corrected dissociation energies of the six most stable ML-(methanol)<sub>2</sub> conformers are summarized in Table 2, together with their Boltzmann factors at 298 K. Again, single point MP2 energies were calculated and the results are also included in Table 2. Similarly, the eight quaternary ML-(methanol)<sub>3</sub> conformers were identified and their geometries are given in Figure 3.8, while the related raw and the BSSE and ZPE corrected dissociation energies and the Boltzmann factors are given in Table 2, together with their single point MP2 energies. In these eight structures, **ML-3m-II, III, IV,**

V and VI each has a cooperative H-bonded ring formed with the OH functional groups of the ML and the three methanol molecules.

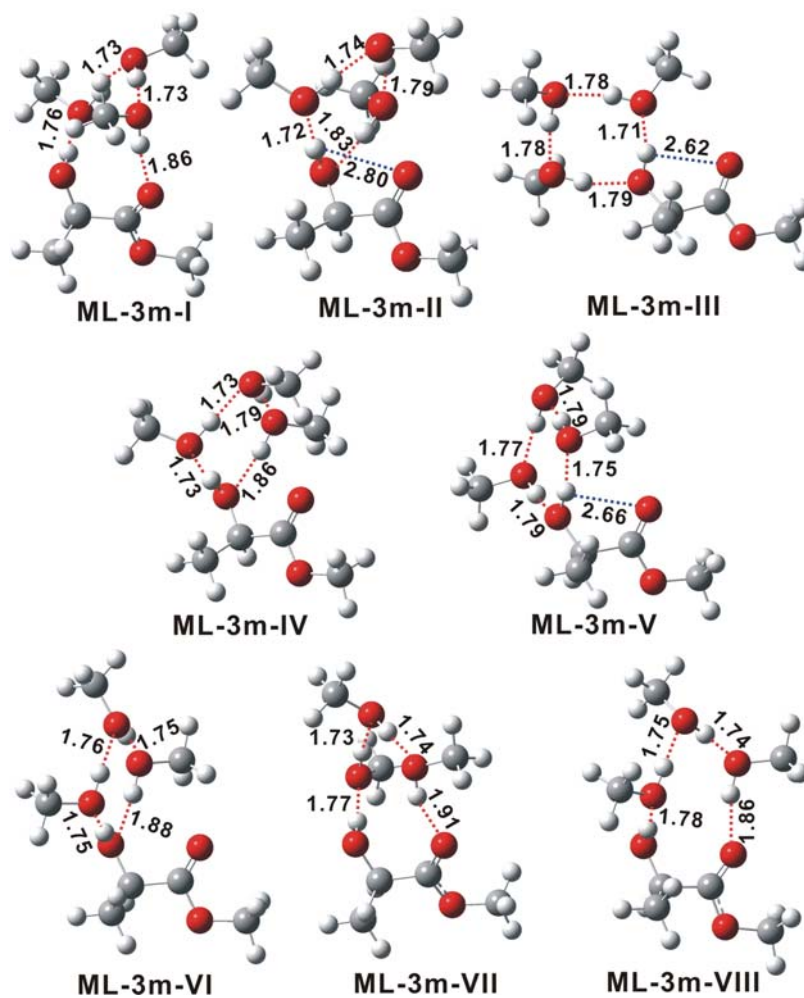


Figure 3.8 Optimized geometries of the six most stable 1:3 ML-methanol conformers. The intermolecular and the (secondary) intramolecular hydrogen bond lengths are in the unit of Å. Any potential secondary intramolecular hydrogen bond with a length longer than  $\sim 3$  Å is not shown.

The C=O functional group of ML is not involved in the intermolecular H-bonds and the intramolecular H-bond between C=O and OH of ML is significantly weakened. One may therefore expect that the C=O stretching bands of these conformers experience blue shifts compared to the corresponding ML monomers. It is also interesting to point out that the single point MP2 relative energies of these quaternary conformers show substantial changes from the corresponding DFT energies, resulting in noticeable different stability ordering as compared to the DFT ordering. In particular, the structures with the cooperative H-bonds become more preferentially favored with the MP2 energies versus the other structures. The related changes from DFT to MP2 for the 1:2 ternary clusters are much smaller, as are the cases for the 1:1 binary complexes discussed previously.

For the ML dimer, extensive geometry searches for the ML dimer had been performed previously by Borho and Suhm.<sup>12</sup> Based on their results, only two lowest energy conformers have appreciable population at room temperature. These two most stable (ML)<sub>2</sub> conformers were re-optimized with the larger basis set used here. The resulting binary geometries are given in Figure 3.2 and the corresponding DFT and MP2 energies and Boltzmann factors are listed in Table 2.

### **3.4.3 Comparison of the experimental and simulated VA and VCD spectra**

The Boltzmann factors based on the MP2 energies were used to calculate the

population weighted VA and VCD spectra for each species, i.e. ML, ML-(methanol)<sub>1,2,3</sub> and (ML)<sub>2</sub>. The resulting VA and VCD spectra for each species are summarized in Figure 3.9. The VA spectrum of each species exhibits subtle differences. For example, the ML-3m species has a doublet signature at the C=O stretching region, with one of doublet being noticeably *blue* shifted from that of the ML species. The VCD spectral signatures for these species, on the other hand, are significantly different. This makes it possible to interpret the experimental spectra using the calculated results with fairly high confidence. The ab initio calculations performed here, however, do not provide direct information about the relative abundance of each species in the 2M ML solutions in either methanol or CCl<sub>4</sub>. The VA and VCD spectral features observed experimentally were used to guide our estimation of the relative abundance of them in each solution, together with the information obtained from the MD simulations. For example, the contribution from the (ML)<sub>2</sub> species to the experimental VA and VCD spectra of 2M ML in methanol is expected to be quite small based on the MD simulation results. Also from the MD simulation, the contribution from the (ML)<sub>2</sub> species is anticipated for the 2M ML in CCl<sub>4</sub>, whereas that from the larger ML self-aggregates is predicted to be small.

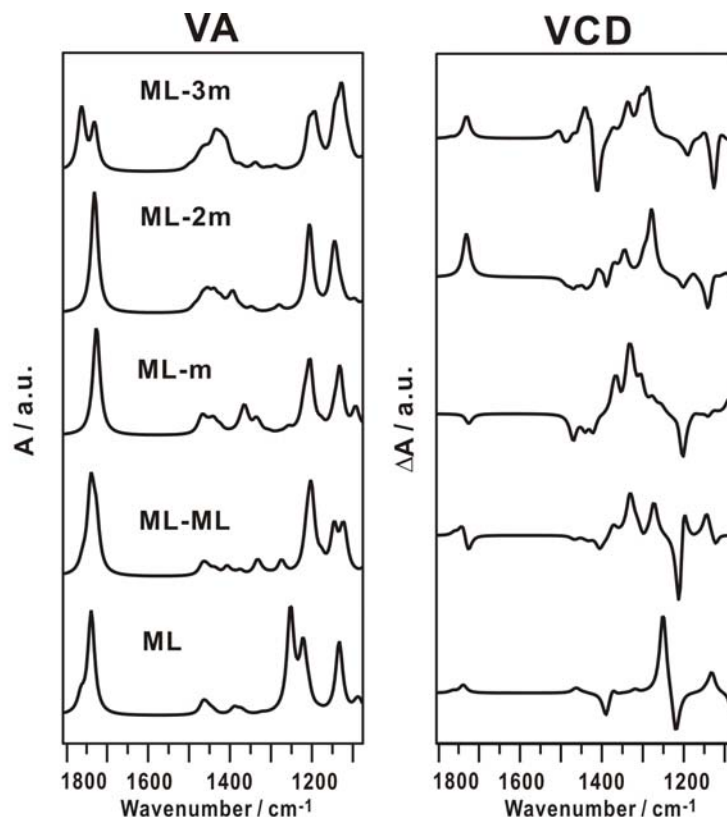


Figure 3.9 Calculated population weighted VA and VCD spectra of the ML monomer, the ML dimer, and the ML-(methanol)<sub>1,2,3</sub> clusters, at the B3LYP/6-311+G\*\* level of theory. The Boltzmann factors calculated from the single point MP2 energies are used for the population weights.

For the 2M ML in CCl<sub>4</sub>, the situation is straightforward since only ML and (ML)<sub>2</sub> are expected to be dominant. The ML monomeric species and the ML-ML species with an estimated relative abundance of 65% and 35%, respectively, were used to simulate the experimental spectra. The comparison of the experimental and the simulated 2M ML in CCl<sub>4</sub> are summarized in Figure 3.10. As one can see,

the predicted VA and VCD spectra closely resemble the experimental ones. Not only the peak positions but also the relative peak intensities are satisfactorily captured by the simulation. For the 2M ML in methanol, the situation is somewhat more complicated. The comparison of the calculated and the experimental spectral features show that there are clearly contributions from the ML and the 1:1 ML-m species. Another main point for consideration is the unusual blue shifted C=O band observed. Such blue shifted C=O bands had been detected before in the matrix isolation studies of 1:1 HCl-methyl acetate<sup>29(a)</sup> and HF-methyl acetate<sup>29(b)</sup> complexes where it was interpreted as an alkoxy structure with HCl H-bonded to the ester oxygen or a Fermi resonance between the displaced  $\nu$  (C=O) and  $2\nu$  (C=C), respectively. The ab initio calculations performed for the ML-m species show that they have a red shifted C=O band compared to the ML monomer. In addition, the preliminary matrix isolation experiment performed for the 1:1 ML-m species showed clearly a red shifted C=O band. The 1:1 binary ML-m species therefore cannot be responsible for the blue shifted C=O band observed in the 2M ML in methanol. As a result, one can speculate that some contributions from the ML-3m species since this is the only species discussed here with a noticeably blue shift. Therefore, an empirical ratio of 15% ML, 55% ML-m and 30% ML-3m was estimated. The simulated and experimental VA and VCD spectra of 2 M ML in methanol are compared in Figure 3.10. As one can see, all major features of the experimental spectra of 2M ML in methanol are captured. It is also interesting to

note that in the case of 2M ML in water, contributions from the quaternary ML-(water)<sub>3</sub> species were also needed to better account for the observed spectral features.

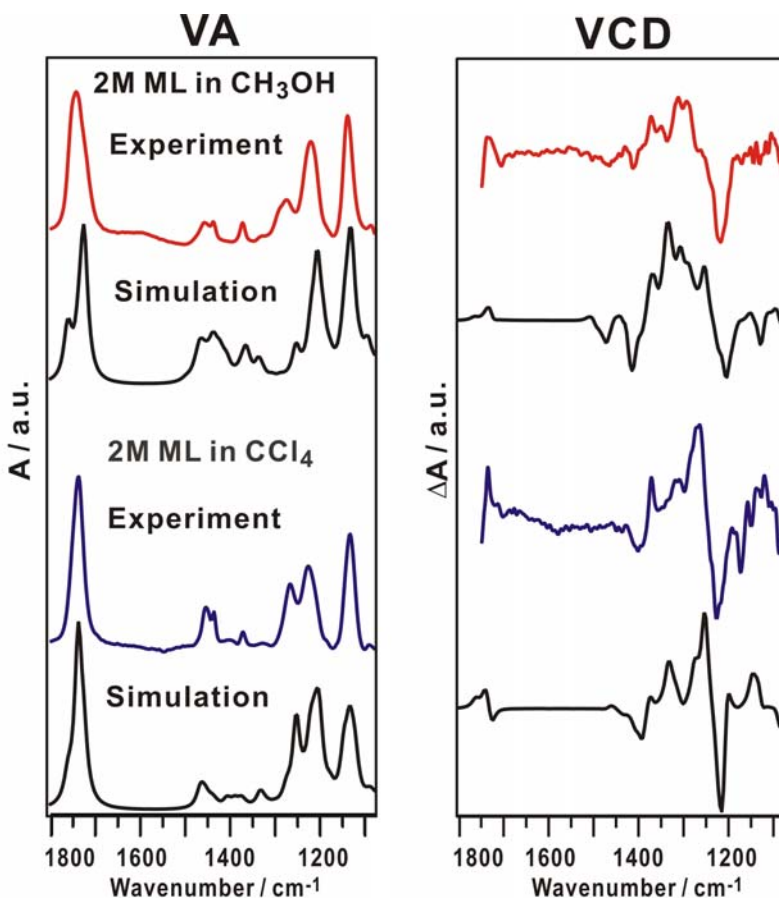


Figure 3.10 Comparison of the experimental VA and VCD spectra of the 2 M ML in methanol with the corresponding population weighted VA and VCD spectra of 15% ML monomer, 55% ML-1m, and 30% ML-3m (top). Comparison of the experimental VA and VCD spectra of the 2 M ML in CCl<sub>4</sub> with the corresponding population weighted VA and VCD spectra of 65% ML monomer and 35% ML-ML (bottom).

### 3.5 Conclusions

The VA and VCD spectra of 2M ML in CCl<sub>4</sub> and methanol solution have been measured for the first time in the 1000-1800 cm<sup>-1</sup> region. The solvent effects on the VA and VCD spectra of ML in CCl<sub>4</sub> and in methanol solutions have been investigated in details by examining the explicit H-bonding between solvent-solute and between solute-solute molecules. Both MD and ab initio DFT and MP2 calculations have been carried out to aid the constructions of the H-bonding species in these two solutions. The population weighted VA and VCD spectra for the ML-(methanol)<sub>1,2,3</sub> and ML-ML species have been simulated and compared to the experimental measurements. The significant changes in both VA and VCD features in these two solutions and with different concentrations have allowed us to evaluate the amount of contributions from these proposed species with good confidence. The results obtained show that it is essential to take into account of the intermolecular H-bonding interactions in order to understand the VA and VCD spectra in solution for chiral molecules and solvent molecules capable of H-bonding interactions. The implicit PCM model, on the other hand, does not generate satisfactory predictions in these cases. In the (ML)<sub>2</sub> and the ML-(methanol)<sub>1,2</sub> clusters, the *insertion* conformers have been found to be much more stable than those with only *additional* H-bonds. For the larger quaternary ML-(methanol)<sub>3</sub> clusters, the cooperative H-bonding involving both ML and methanol molecules have been predicted to become increasingly important.

## References:

- 1 Liu, Y.; Yang, G.; Losada, M.; Xu, Y. *The J. Chem. Phys.* **2010**, *12* 234513
- 2 Eliel, E. L.; Wilen, S.; Doyle, M. P. *Basic Organic Stereochemistry*, Wiley-Interscience: New York, **2001**.
- 3 (a) Müller, T.; Wiberg, K. B.; Vaccaro, P. H. *J. Phys. Chem. A*, **2000**, *104*, 5959; (b) Wilson, S. M.; Wiberg, K. B.; Cheeseman, J. R.; Frisch, M. J.; Vaccaro, P. H. *J. Phys. Chem. A*, **2005**, *109*, 11752.
- 4 Mukhopadhyay, P.; Zuber, G.; Wipf, P.; Beratan, D.N. *Angew. Chem. Int. Ed.* **2007**, *46*, 6450.
- 5 Mukhopadhyay, G.; Zuber, G.; Goldsmith, M. R.; Wipf, P.; and Beratan, D. N. *Chem. Phys. Chem.* **2006**, *7*, 2483.
- 6 (a) Losada, M.; Nguyen, P.; Xu, Y. *J. Phys. Chem. A*, **2008**, *112*, 5621; (b) Su, Z.; Xu, Y. *Angew. Chem.* **2007**, *119*, 6275; (c) Su, Z.; Xu, Y. *Angew. Chem. Int. Ed.* **2007**, *46*, 6163; (d) Su, Z.; Wen, Q.; Xu, Y. *J. Am. Chem. Soc.* **2006**, *128*, 6755.
- 7 He, J.; Polavarapu, P. J. *J. Chem. Theory Comput.* **2005**, *1*, 506.
- 8 (a) Yang, G.; Xu, Y. *Phys. Chem. Chem. Phys.* **2008**, *10*, 6787; (b) Lasada, M.; Tran, H.; Xu, Y. *J. Chem. Phys.* **2008**, *128*, 014508.
- 9 (a) Yang, G.; Xu, Y. *J. Chem. Phys.* **2009**, *130*, 164506; (b) Losada, M.; Xu, Y. *Phys. Chem. Chem. Phys.* **2007**, *9*, 3127.
- 10 Sadlej, J.; Dobrowolski, J. C.; Rode, J. E. *Chem. Soc. Rev.* **2010**, *41*, 35.
- 11 (a) Pohl, G.; Perczel, A.; Magyarfalvi, G.; Vass, E.; Tarczay, G. *Phys. Chem. Chem. Phys.* **2007**, *9*, 4698; (b) Tarczay, G.; Góbi, S.; Magyarfalvi, G.; Vass, E. *Vibrational Spectroscopy*, **2009**, *50*, 21.
- 12 (a) Borho, N.; Suhm, M. A. *Org. Biomol. Chem.* **2003**, *1*, 4351; (b) Fárník, M.; Weimann, M.; Steinbach, C.; Buck, U.; Borho, N.; Adler, T. B.; Suhm, M. A. *Phys. Chem. Chem. Phys.* **2006**, *8*, 1148; (c) Adler, T. B.; Borho, N.; Reiher, M.; Suhm, M. A. *Angew. Chem. Int. Ed.* **2006**, *45*, 3440; (d) Borho, N.; Suhm, M. A.; Le, K. Barbu-Debus and A. Zechnacker, *Phys. Chem. Chem. Phys.* **2006**, *8*, 4449; (e) Barbu-Debus, L. K.; Broquier, M.; Mahjoub, A.; Zehnacker-Rentien, A. *Phys. Chem. Chem. Phys.* **2009**, *11*, 7589.
- 13 Zehnacker, A.; Suhm, M. A. *Angew. Chem. Intl. Ed.* **2008**, *47*, 6970.
- 14 (a) Borho, N.; Xu, Y. *Phys. Chem. Chem. Phys.* **2007**, *9*, 1324; (b) Ottaviani, P.;

- Velino, B.; Caminati, W. *Chem. Phys. Lett.* **2006**, *428*, 236.
- 15 Borba, A.; Gómez-Zavaglia, A.; Lapinski, L.; Fausto, R. *Vib. Spectrosc.* **2004**, *36*, 79.
- 16 Warner, J. C.; Cannon, A. S.; Dye, K. M. *Environ. Impact Assess. Rev.* **2004**, *24*, 775.
- 17 (a) Aparicio, S. *J. Phys. Chem. A* **2007**, *111*, 4671; (b) Aparicio, S.; Alcalde, R. *Green Chem.* **2009**, *11*, 65.
- 18 Losada, M.; Xu, Y. *Phys. Chem. Chem. Phys.* **2007**, *9*, 3127.
- 19 Case, D. A.; Darden, T. A.; Cheatham, T. E.; Simmerling, C. L. et al., AMBER 9 University of California, Berkeley, **2006**.
- 20 Ding, G. D.; Karasawa, N.; Goddard, W. A. *J. Chem. Phys.* **1992**, *97*, 4309.
- 21 Essmann, U.; Perera, L.; Berkowitz, M. L.; Darden, L.; Lee, H.; Pedersen, L. G. *J. Chem. Phys.* **1995**, *103*, 8577.
- 22 Ryckaert, J. P.; Ciccotti, G.; Berendsen, H. J. C. *J. Comput. Phys.* **1977**, *23*, 327.
- 23 Frisch, M. J.; Trucks, G. W.; Schlegel, H. B. et al., Gaussian 03, Revision B.01, Gaussian, Inc., Pittsburgh Pennsylvania, **2003**.
- 24 (a) Becke, A. D. *J. Chem. Phys.* **1993**, *98*, 5648; (b) Lee, C. T.; Yang, W. T.; Parr, R. G. *Phys. Rev. B*, **1988**, *37*, 785 .
- 25 Van Duijneveldt, F. B.; Van Duijneveldt-van de Rijdt, D. J.; Van Lenthe, J. H. *Chem. Rev.* **1994**, *94*, 1873.
- 26 Boys, S. F.; Bernardi, F. *Mol. Phys.* **1970**, *19*, 553.
- 27 (a) Miertus, S.; Scrocco, E.; Tomasi, *J. Chem. Phys.* **1981**, *55*, 117; (b) Tomasi, J.; Persico, M. *Chem. Rev.* **1994**, *94*, 2027; (c) Cramer, C.; Truhlar, D. *Chem. Rev.* **1999**, *99*, 2161.
- 28 (a) Guardia, E.; Marti, J.; Garcia-Tarres, L.; Laria, D. *J. Mol. Liq.* **2005**, *117*, 63; (b) Kongsted, J.; Mennucci, B. *J. Phys. Chem. A*, **2007**, *111*, 9890; (c) Malaspina, T.; Fileti, E. E.; Rivelino, R. *J. Phys. Chem. B*, **2007**, *111*, 11935.
- 29 (a) Maesx, G.; Smolders, A.; Vandevyvere, P.; Vanderheyden, L.; Zeegers-Huyskens, Th. *J. Mol. Struct.* **1988**, *173*, 349; (b) Patten, K. O. Jr.; Andrews, L. J. *Phys. Chem.* **1986**, *90*, 1073.

## **Chapter 4 VCD spectroscopy of chiral molecular system in cold rare gas matrices**

In this chapter, I describe the experimental efforts I have made to combine the VCD spectroscopy with the matrix isolation technique in order to study hydrogen-bonded complexes formed in a cold rare gas matrix. In the first section, I cover some properties of rare gas matrices that are relevant to my research work and the experimental difficulties along with discussions of possible solutions. In the second part I will summarize the preliminary VCD measurements of methyl lactate obtained in the Ar matrix. Last but not the least, it will be followed by some concluding remarks.

### **4.1 Introduction**

This introduction includes two parts. One is about some general properties of the rare gas matrices, which are relevant to my research system. The other part is the introduction of some previous experiments followed by some comparison and analysis to my own experiments.

#### **4.1.1 Introduction to some general properties of the rare gas matrices<sup>1</sup>**

The rare gas matrices are commonly used in infrared spectroscopy for the studies of molecular complexes, especially hydrogen-bonded complexes.<sup>2</sup> In general, one needs to consider purity, transparency, inertness, rigidity, volatility,

heat of fusion, lattice energy and thermal conduction to select a good candidate for a matrix. Below I briefly review these seven categories.

#### **4.1.1.1 Purity**

Purity is one key property. In the matrix isolation experiment, it is highly desirable to select the matrix material of the highest purity available.

Table 4.1 Typical research grade gases Ar, N<sub>2</sub> and O<sub>2</sub> and their respective major impurities in unit of ppm.

	Ar	N <sub>2</sub>	O <sub>2</sub>
Purity(%)	>99.9995	>99.9995	>99.9996
Major impurities in ppm			
Ar	-	<5.0	<15
CO <sub>2</sub>	<0.5	<0.5	<0.5
CO	<1.0	<1.0	<1.0
H <sub>2</sub>	<2.0	<2.0	-
CH <sub>4</sub>	<0.5	<0.5	<0.5
N <sub>2</sub>	<3.0	-	<15
N <sub>2</sub> O	<0.1	<0.1	<0.1
O <sub>2</sub>	<1.0	<1.0	-
H <sub>2</sub> O	<0.5	<0.5	<0.5
Total hydrocarbon	<0.5	<0.5	<1.0

Water has a strong absorption band at about 1600 cm<sup>-1</sup> which is in the finger print region where VCD spectra are collected. Therefore, the water impurity in the host gas should be removed as much as possible. One can do this by passing the

gas through a "cold finger", which could be copper coils or glass tubes immersed in the liquid nitrogen. Alternatively, it can be done by passing the rare gas through a column packed with effective drying agents, such as NaOH. The latter is the method adopted in my research work.

#### **4.1.1.2 Transparency**

As in the cases of liquid solvents, the matrix material chosen should not have strong absorptions in the region of interest. In addition, the matrix film deposited on the cold optical window often shows appreciable scattering effect, causing a significant loss of light power. It is therefore important to apply deposition techniques which can generate a matrix with as little scattering effect as possible. This is particularly important in MI-VCD, since the VCD measurements have a stringent requirement on the minimum amount of light which reaches the detector. A rough matrix film which has severe scattering effects is detrimental to the MI-VCD experiments. Two main factors in the preparation of the matrix film are crucial: the flow rate and the deposition period. By using a slow flow rate, the molecules can be distributed on the cold window more evenly. Therefore, the slower the flow rate, the smoother the surface of matrix film would be. A longer deposition period results in a thicker matrix film which tends to be rougher on the surface. In general, a thinner layer is better in terms of energy loss. However, a thin layer also means that less samples have been deposited. In this case, one may have

too little sample to obtain a VA spectrum with the desirable intensity for optimum VCD experiments. Moreover, the temperature of the matrix also plays an important role in the scattering effect since it changes the refractive index of the film. For example, xenon is reasonably transparent when deposited at 66K but when the temperature cools down to 50K, the xenon matrix becomes highly scattering.<sup>1</sup>

#### **4.1.1.3 Inertness**

Matrix materials should be chemically stable and inert to the guest molecules, since the last thing we want to see is a reaction between them. The main point of MI experiment is to establish a system providing an insulating environment which can keep the guest molecules stable and isolated. But all matrices perturb the energy levels of the trapped species and to some extent modify the vibrational frequencies.

#### **4.1.1.4 Rigidity**

Rigidity is the ability of the matrix to accommodate the solute molecules in the lattice. If it is not rigid enough, the solute molecules can diffuse in the matrix and aggregate with each others. The most important factor on the rigidity is the temperature. The pioneer work by Pimentel provides a rough guide which states that the matrix temperature should be at least half of its melting point  $T_m$ .<sup>1</sup>

Similarly, Tammann's rule says that  $T_d$ , at which diffusion first becomes significant for salts and oxide is  $T_d \approx 0.57T_m$  and for covalent compounds is  $T_d \approx 0.90T_m$ .<sup>3</sup> For this reason, the application of nitrogen cryostats turns to be very limiting in terms of the possible matrix materials since it can only cool down to 77K. Temperature properties of some common matrix materials are summarized in the Table 4.2, where m.p. And b.p. represent melting point and boiling point.

Table 4.2. Thermal properties of some common matrix materials.

	Td(K)	m.p.(K)	b.p.(K)
Ne	10	24.6	27.1
Ar	35	83.8	87.3
Kr	50	115.8	119.8
Xe	65	161.4	165.1
CH <sub>4</sub>	45	90.7	111.7
N <sub>2</sub>	30	63.2	77.4
O <sub>2</sub>	26	54.4	90.2
CO	35	68.1	81.6
CO <sub>2</sub>	63	216.6	194.6

#### **4.1.1.5 Volatility**

For practical reasons, the matrix material should be in the gas phase at room temperature so that it can be handled in vacuum line. Ideally, after deposition it should remain on the cold window under a vacuum of  $10^{-4}$  mm Hg or 10 mTorr. The upper limit is  $10^{-3}$  mmHg or 100 mTorr. To achieve this, a very low temperature cryostat is required. If this requirement is not fulfilled, it will cause a severe heat leak, raise the temperature of the deposited layers, and impair the vacuum environment. During the annealing procedure, it happened a few times when I raised the temperature a bit too high and lost control of the vacuum condition. When the vacuum is lost, the temperature in the cryostat will rise up. When this happens, a thin layer of water condensed from atmosphere can often be observed on the outer shroud due to the heat leak.<sup>3</sup>

Table 4.3. The temperatures of some common matrix materials at the vapor pressure of 100 mTorr.

Material	Temp. / K
Ne	11
Ar	39
Kr	54
Xe	74
CH <sub>4</sub>	48
N <sub>2</sub>	34
O <sub>2</sub>	40
CO	38
CO <sub>2</sub>	106

These temperatures are all slightly higher than the T<sub>d</sub> values in the Table 4.2. Therefore, it is the matrix rigidity which determines the upper limit of the allowed temperature rather than the volatility.

#### 4.1.1.6 Heat of fusion and lattice energy

When the matrix material condensed on the cold window from the room

temperature gas, energy is given out. This energy is termed as heat of fusion. The rate of fusion energy is determined by the deposition rate. It should not exceed the cooling power of the cryostat. Otherwise, the energy will be accumulated on the surface of the matrix to create significant diffusions. The solid matrix material can form certain lattice structures. More details about the structure are given in the next section. The most important thing of the lattice is its energy which is called lattice energy. It is defined as the energy required for forming a lattice at 0 K. It can also be seen as the energy required to remove a molecule from its place in the lattice. The higher the lattice energy is, the higher  $T_d$  is. Usually the zero point energy is much smaller than the heat of sublimation, therefore it can be ignored. However, this is not the case for light noble gases such as neon and argon, whose zero point energy is relatively larger. Table 4.4 lists the heat of fusion and lattice energy of some common matrix materials.

Table 4.4. Heat of fusion and lattice energies of some common matrix materials

	Heat of fusion (J/mol)	Lattice energy (J/mol)
Ne	335	1874
Ar	1190	7724
Kr	1640	11155
Xe	2295	16075
CH <sub>4</sub>	971	-
N <sub>2</sub>	721	6904
O <sub>2</sub>	444	-
CO	836	7950
CO <sub>2</sub>	8339	26987

#### 4.1.1.7 Thermal conductivity

As the layers of matrix grow thicker on the cold deposition window, the heat dissipation on the surface of the matrix must pass through those layers to the cold window (or plate). If the thermal conduction is poor, the energy will be contained on the surface to create the so called "local heating". This can lead to many undesirable situations, such as scattering and loss of solutes monomers. The key to avoid this is to deposit slowly. That also means the better conductivity of the

matrix material, the faster the deposition can go. The common unit of the thermal conductivity is  $\text{W m}^{-1}\text{K}^{-1}$ , which means how much power can be conducted through unit thickness per Kelvin.

Table 4.5. Thermal conduction properties of some common matrix materials.

Material	$\text{W m}^{-1}\text{K}^{-1}$ at 20K
Ne	0.4
Ar	1.3
Kr	1.2
Xe	2
CH <sub>4</sub>	0.1
N <sub>2</sub>	0.4

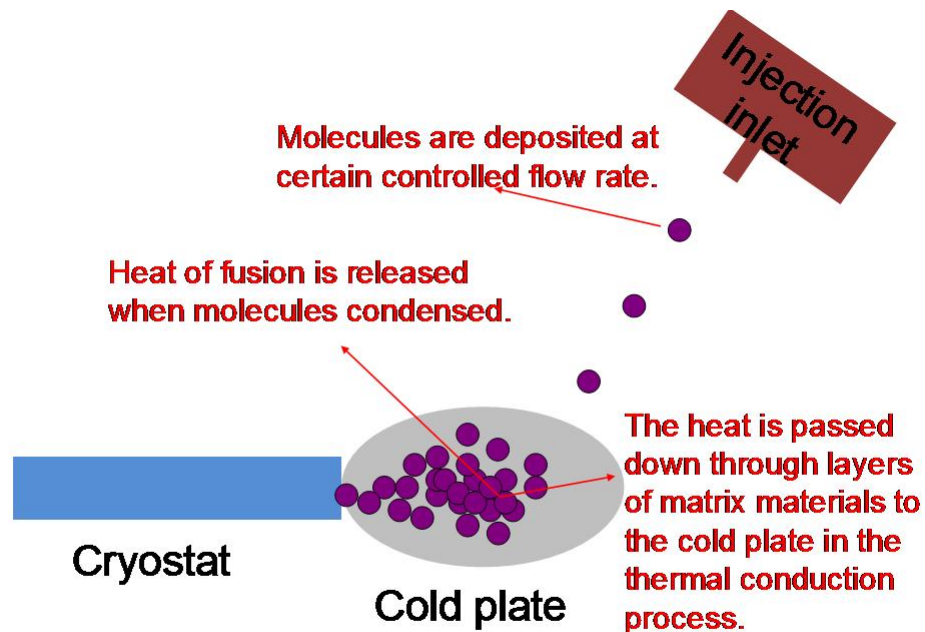


Figure 4.1 The graphical demonstration shows how the matrix material condenses on the cold plate.

#### 4. 1.1.8 Crystal structures

All the noble gas matrix materials are spherical in shape. The solid made of spherical molecules with non-directional bond is generally “close-packed” in structure. This mechanism maximizes the number of nearest neighbors, which give the maximum intermolecular interactions and stabilize the matrix. There are two different types of close-packed structures. One is hexagonal close-packed structure and the other is cubic close-packed structure. Both are very efficient in terms of space utilization.

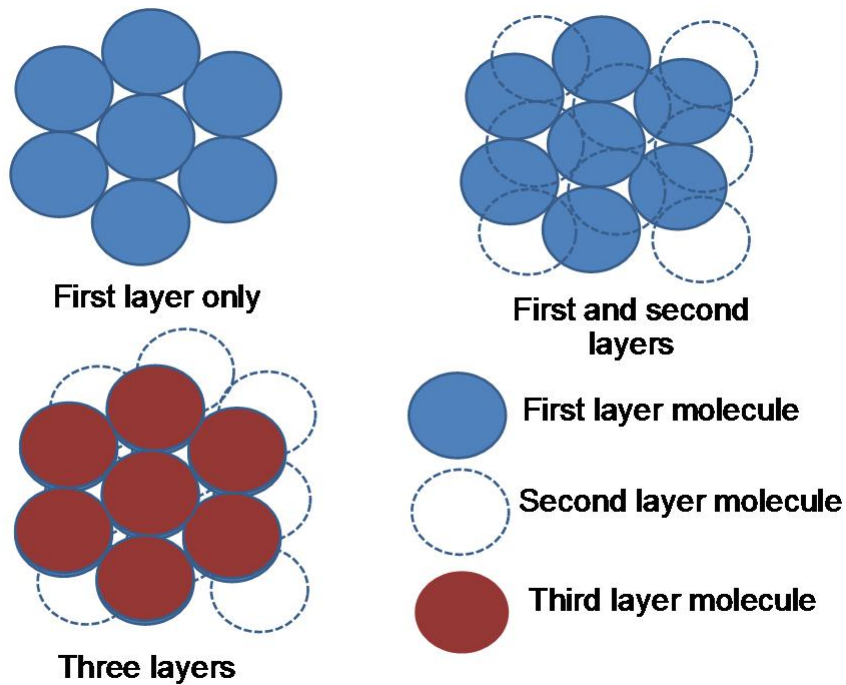


Figure 4.2. Hexagonal close-packed structure lattice of noble gas (figure adapted from ref 1).

In the hexagonal close-packed structure lattice, each molecule has six neighbors in the same plane. The solid molecules composed the first layer and dashed line molecules nestle right on top of the depressions of the first layers. The third layer sits on top of the depression of the second layers and if looking down from top, it superimposed with the first layer.

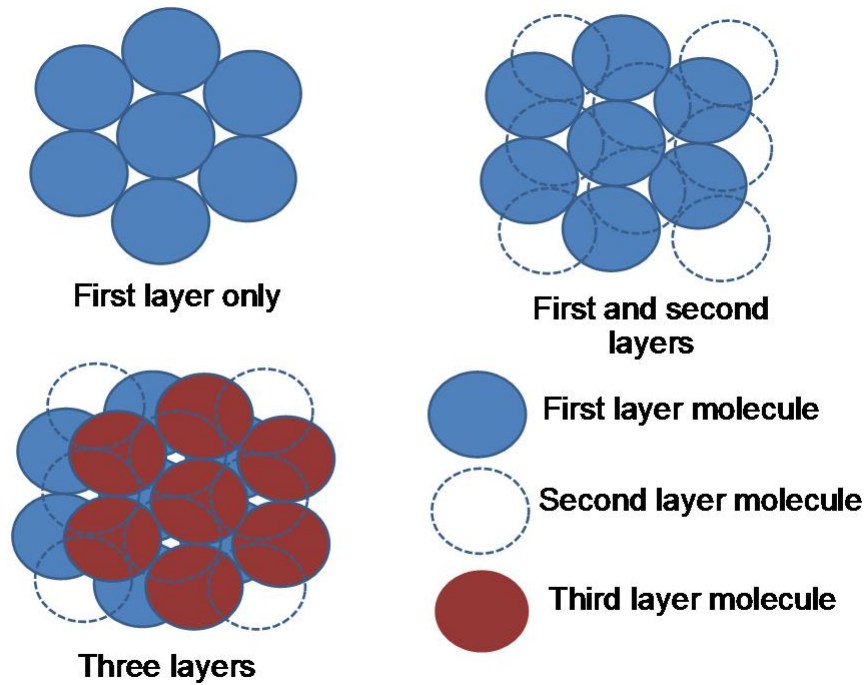


Figure 4.3 The structure of cubic close-packed structure lattice of noble gas (figure adapted from ref 1).

In the cubic close-packed structure lattice, except for the identical first two layers to the hexagonal structure, the third layer doesn't stack on the depressions of the second layer but nestles on the depressions of the whole thing. The subtle differences can be viewed another way as that the center of third layer molecules cover the tetrahedral holes in hexagonal structure and cover the octahedral holes in the cubic close-packed structures.

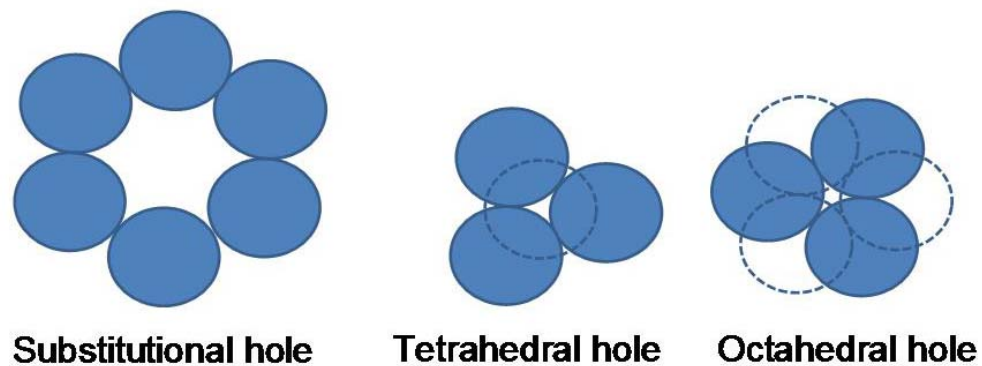


Figure 4.4. The structures of substitutional holes, tetrahedral holes and octahedral holes (figure adapted from ref 1).

There are three sizes of holes which can accommodate guest molecules. The geometries of those holes are of importance to matrix studies in relation to analyze the spectrum. The biggest hole is the substitutional hole which has the equivalent diameters as the matrix materials. Nevertheless for the other two types, the tetrahedral hole can hold molecules with 0.225 diameters of the matrix materials and the octahedral hole can contain molecules as large as 0.414 diameter. If the guest molecules are much smaller than the trapping holes, then the smaller matrix material should be considered.

Table 4.6 Trapping site diameters ( $10^{-10}$  m) for some common matrix material at 4K.

	Substitutional	Octahedral	Tetrahedral
Ne	3.156	1.31	0.71
Ar	3.755	1.56	0.85
Kr	3.992	1.65	0.9
Xe	4.336	1.81	0.97
CH <sub>4</sub>	4.147	1.73	0.94
CF <sub>4</sub>	4.761	-	-

#### 4.1.2 Previous experiment study and analysis of experimental chanelleges

In this section, the pioneer work of VCD measurements in matrix is reviewed first. Since VCD is quite vulnerable to artifacts, the sources of artifacts of VCD in the solution phase are discussed, followed by the specifics related to MI-VCD measurements.

VCD is very sensitive to the structural dihedral angles, therefore VCD bands of different conformations often show different spectral features even opposite signs. More over, the solute-solute and solute-solvent interaction, especial H-bonding interactions can modify the conformational distribution and result in

shifts of vibrational bands and alternation in their intensities. These effects sometimes lead to a blurry and featureless spectrum. As a result, very limited information can be extracted.

In the early 1980s, Stephens' group first performed the VCD measurements at cryogenic temperature and showed that the spectrum line widths were greatly reduced.<sup>4</sup> The host matrix material used was argon as since it has minimum perturbations of the guest molecules. The guest molecules used are  $\alpha$ - and  $\beta$ -pinene since they are rigid and have a single conformation in each case. This makes the experiment interpretations straightforward. Comparison between the matrix and the solution measurement in  $\text{CCl}_4$  were also done. Experimentally, they only focused on the C-H stretching region and found that the VCD signals of the + and - ( $\alpha$ -, $\beta$ -) pinene are exact mirror images to each other and the racemic pinenes showed no features in the spectra as expected. These experiments demonstrate the validity of using matrix isolation technique in VCD measurements. In addition, they also showed some advantages with MI-VCD measurements as compared to the more traditional solution VCD measurements. The band widths in matrices are typically of  $4\sim 5\text{ cm}^{-1}$ , as compared to  $8\text{ cm}^{-1}$  or larger in the solution. More importantly, the intensities of VCD can also be enhanced substantially.

A few years later, Polavarapu's group continued this area of research by applying a Fourier transform VCD spectrometer to perform MI-VCD experiments.

<sup>5</sup> Using the pulsed spray method instead of slow spray method for deposition and changing the host matrix material from argon to nitrogen gas since they found the latter is more transparent, the authors were able to perform VCD measurement in the region of  $1600\text{ cm}^{-1}$  to  $800\text{ cm}^{-1}$ . The absorptions of pinenes are much weaker in this region than the C-H stretching region and the spectrum resolution of  $1\text{ cm}^{-1}$  was achieved.

A long dry period of the MI-VCD experiments followed. In 2005, a Hungarian group published their work on two highly flexible molecules, 2-amino-1-propanol and alaninol.<sup>6</sup> Each of them has more than 25 conformers at room temperature as predicted by *ab initio* calculations. The much higher resolution achieved with the MI-VCD measurements permitted the reassignment of the most abundant conformational species in the previous studies of the same molecules in solution.<sup>7</sup>

VCD measurements are quite prone to artifacts. In general, the major sources of artifacts originate from strains and polarization sensitivities of optical components in the optical train used in the experiments. Another source of artifacts is from the sample, especially when it is in matrix. The matrix deposited on a cold plate can have strains and polarization sensitivity. Compared to the matrix film, the sample in the solution phase has consistent artifacts and can be reproduced in each experiment, therefore can be subtracted accordingly. But in matrix isolation experiments, the strains and sensitivities can vary a lot depending

on how the matrix film is prepared. Experimental factors such as flow rate, deposition period, annealing temperature, and optical alignment of the cold head, can all have strong effects.

The best way to correct for VCD artifacts for solution measurements is to measure the raw VCD spectra of both enantiomers if available, then subtract the two spectra and divide it by 2.<sup>8</sup> Another common way to correct for artifacts is to use one enantiomeric sample and a racemic sample, then subtract the two raw spectra to obtain the desired VCD spectrum. Similar procedure was used by Stephens and Pavalapu's group for their MI-VCD measurements of pinenes, which are rigid and have a single conformer. It is interesting to note that the Hungarian group did not follow this routine, although both enantiomers and the racemic sample are available. One reason is that it is highly challenging to make the same matrix for subsequent measurement of the opposite enantiomer or racemic sample. Instead, these authors assumed that the VCD baseline is at zero if there is no VA absorption. Whether this approach is sound or not is still to be further tested.

In 2008, Nafie's group performed a series of VCD experiments in solution phase to systematically demonstrate how to remove artifacts from the VCD spectra using some additional optical components.<sup>8</sup> First, they introduced a secondary photo elastic modulator (PEM) after the sample and before the detector to reduce linear birefringences associated with the components in the optical train

except samples. Then they adopted the Hug's "virtual enantiomers" method used in the Raman optical activity measurements, which equipped two rotating half wave plate before and after samples. Unfortunately, these new setups are not currently available in our laboratory. Much of my research efforts have been devoted to create identical matrix films for the enantiomer pairs in order to apply the common correct method for VCD spectra.

## **4.2 Experiments and Discussions**

Methyl lactate in  $\text{CCl}_4$  and in methanol solution has been successfully studied (see Chapter 3). The MI-VCD technique allows some control of the specific chiral solute-solvent complexes generated, unlike in a solution where one has essentially no control of that. Furthermore, the much higher spectral resolution with a matrix will allow one to study specific chiral solute-solvent complex in isolation and in detail.

To obtain a good VCD spectrum starts with a good VA spectrum. Comparing to MI-VCD experiments, VA-MI experiments are less complicated, much more robust, i.e., much less sensitive to minor changes in the experimental conditions. I have spent six months to assemble the matrix isolation apparatus from scratch and performed extensive testing runs to validate its proper function.

At the beginning of the experiments, I noticed that there is substantial amount of water. Initially, I suspected that the source of water was from the

FTIR-VCD chambers. After ensuring the proper usage of desiccant and dry nitrogen purging gas for the chambers, I found that the water spectral feature persisted. Another possible source is the argon gas. Although we used the highest standard argon gas, it is still too wet for the MI experiments. Therefore a drying bottle with NaOH pellets was attached to the injection line to remove much of the water, although a trace amount of it remained.

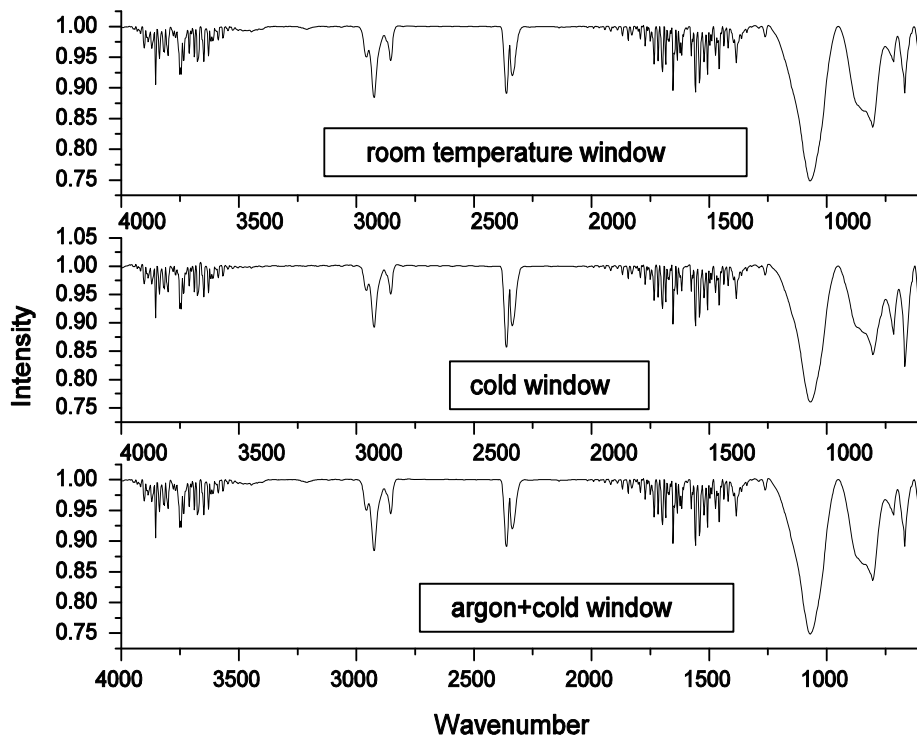
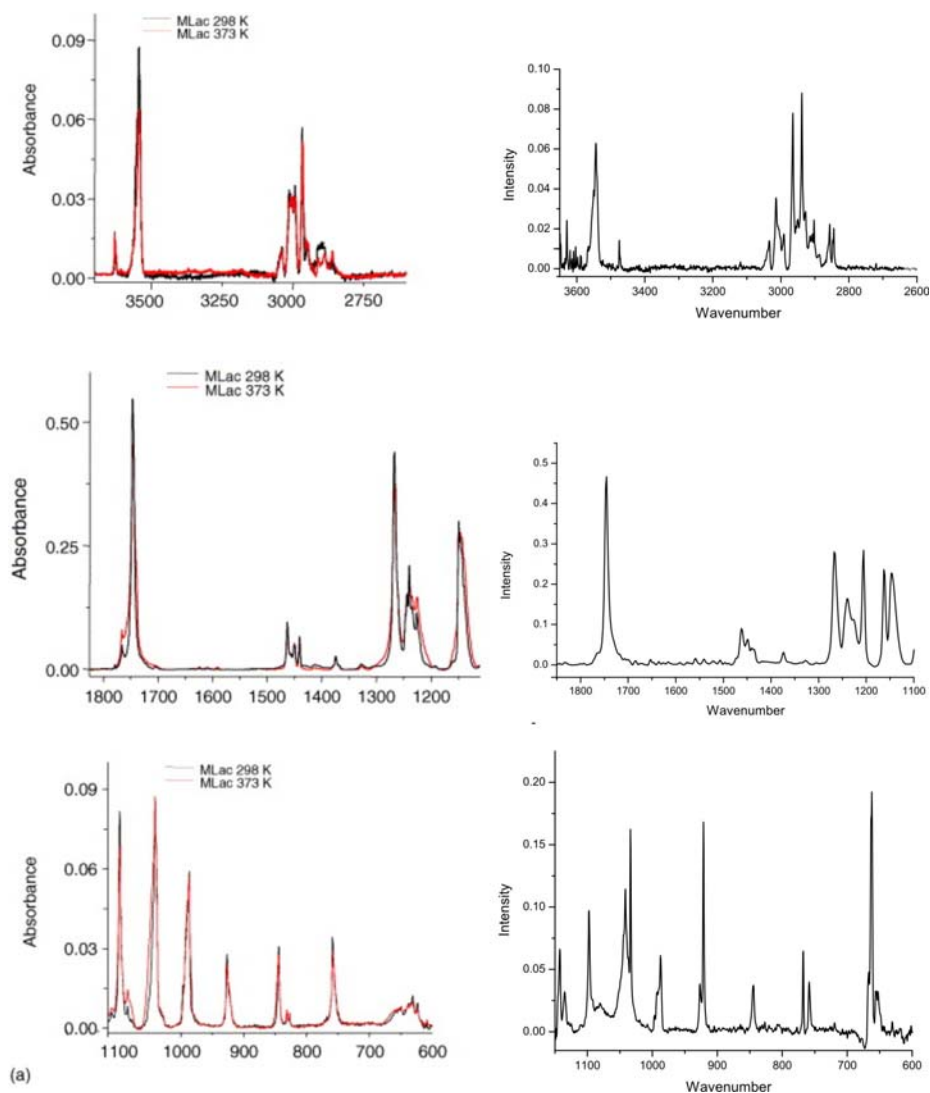


Figure 4.5 Three spectra of MI-IR experiments with cryostat at room temperature, 13K in ultrahigh vacuum condition and with argon deposition for 2 hours to demonstrate the how dry the argon gas after introducing the drying bottle.

The sharper spectral features in the  $3300\text{ cm}^{-1}$  OH stretching region and around  $1650\text{ cm}^{-1}$  HOH bending region are due to the gas phase water inside the instrument chambers. All the other peaks are resulted from the optical components. These water bands and the background peaks can be subtracted easily. The middle graph is the MI experiment at the 13K. Since the cryostat is completely isolated from the chamber, lowering the temperature in the high vacuum condition inside the cryostat should not matter. This is exactly what we observed. The bottom graph is from the experiment at 13 K, but with 2 hours of argon deposition at the flow rate of 0.5 sccm (standard cubic centimeter). The intensity of the water absorption region becomes much smaller compared to what it was before without the drying bottle. Only a trace amount remained compared to the top graph and no other impurities were introduced.

Next, I tried to repeat the VA-MI experiment of methyl lactate reported by Frausto and co-workers<sup>9</sup> and the acetone-methanol complexes detected in argon matrix.<sup>10</sup> According to the publication, the pressure of argon gas should be at least 300 fold larger than the guest molecules like acetone and methanol and the suggested flow rate was 0.6 mmol/hour, which is equal to 0.5 sccm in our case. Since their molecule is comparable to the size of methyl lactate molecule, their experiment conditions are good starting points for us.



(a)

Figure 4.6 The spectra are divided into three regions:  $2500\text{cm}^{-1}$ - $3700\text{cm}^{-1}$ ,  $1000\text{cm}^{-1}$ - $1850\text{cm}^{-1}$  and  $1100\text{cm}^{-1}$  - $600\text{cm}^{-1}$ . The spectra on the left is from literature and on the right is from my experiments. (the left part of the figures is taken from the references 8 for comparison)

Comparing to the literature, my spectra have several additional features. The top graph has an extra peak at  $3480\text{cm}^{-1}$ ; the middle graph has additional peaks at

1210  $\text{cm}^{-1}$  and 1180  $\text{cm}^{-1}$ ; the bottom graph takes several sharp peaks at 1040 $\text{cm}^{-1}$ , 930  $\text{cm}^{-1}$  and 660  $\text{cm}^{-1}$ . These additional features may attribute to either impurities, matrix effects, or multiple trapping sites. Many more experiments with variations in flow rate, deposition period, and annealing temperature, had been tried out in my attempts to get rid of these additional shape peaks. We noticed that these additional features sometimes showed and sometimes did not. The exact cause is yet to be identified. The MI-VCD experiment of methyl lactate in the region from 1850  $\text{cm}^{-1}$  to 1000  $\text{cm}^{-1}$  has also been measured. It is compared with the corresponding methyl lactate VCD spectrum in  $\text{CCl}_4$ .

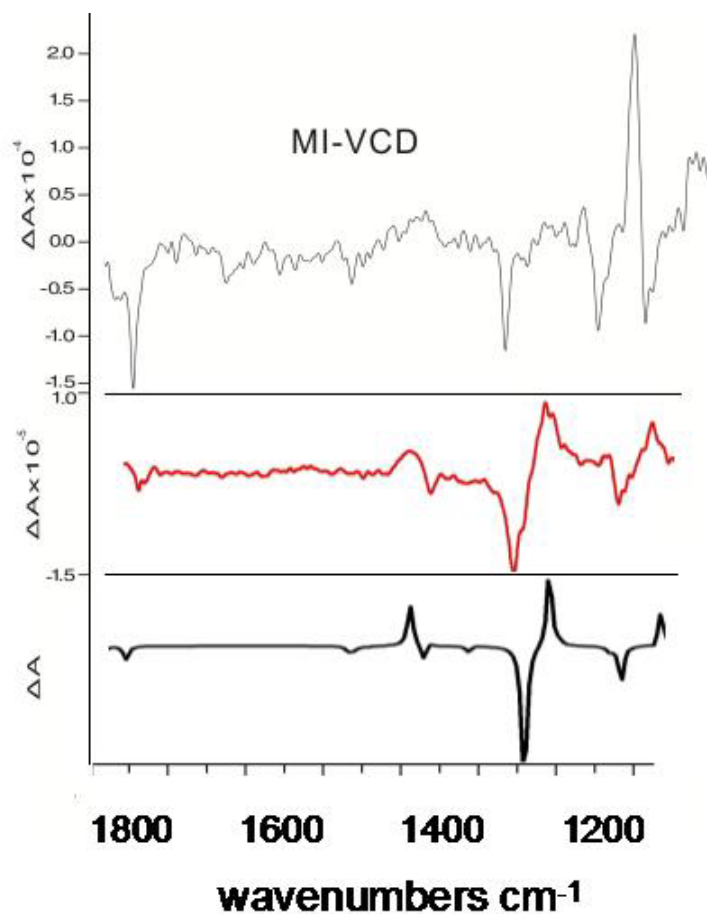


Figure 4.7 Three VCD spectra are compared in this figure. The top graph is the MI-VCD spectrum of methyl lactate with argon matrix; the middle spectrum is methyl lactate in  $\text{CCl}_4$  solution (2M); the last spectrum is theoretical prediction.

The experiment was performed with S-methyl lactate. The signal to noise ratio achieved in the MI-VCD spectrum is not as good as that in solution. But the signal is enhanced by one fold. The MI-VCD spectrum has a FWHH of  $10 \text{ cm}^{-1}$ , where it is  $40 \text{ cm}^{-1}$  in solution for the peaks in the region from  $1250 \text{ cm}^{-1}$  to  $1380 \text{ cm}^{-1}$ . Therefore the advantages of MI-VCD are very obvious. With the

consideration of expected shift from the calculations, the agreement between the experiment and simulation is very well. Later on, the MI-VCD spectrum of R-methyl lactate was also measured. Unfortunately, it does not show good mirror image to the S-methyl lactate spectrum reported here. Since the major artifacts are expected to come from the matrix film deposited on the cold plate. Substantial efforts had been put into getting as good quality matrix film as possible. For example, I deposited with a very slower rate in order to get a smoother film surface. But the trade off is that a long deposition period is needed to have enough samples for measurements. However, the long deposition will make the film less transparent and the light power will be attenuated substantially. This again resulted in a poor signal to noise ratio in the spectrum.

One way to manipulate this is to increase the concentration of methyl lactate in argon. Since the vapour pressure of methyl lactate at the room temperature is 4 Torr. A warm water bath was used to increase its vapour pressure and some heating tapes were wrapped around the injection line to avoid any condensation. Some parts of the injection line tube is of only 1/16 inch outer diameter. Higher temperature tended to cause severe leaks.

#### **4.3 Concluding remarks**

Currently, the MI-VCD experiment of methyl lactate with methanol and water is still on going. But as the difficulties remained in many aspects, we start to

use a more systematical way to solve the problem one by one. First, we begin to use an alternative molecular system, propylene oxide. It has a much high vapour pressure at room temperature. Therefore, a much higher concentration propylene oxide in argon was achieved. The flow rate was 0.5 sccm but the deposition rate was shorten to about 2.5 hours, instead of 10 hours in the case of methyl lactate. Unfortunately, the experimental MI-VCD spectra obtained were still associated with considerable artifacts by comparing the spectra of R- and S-propylene oxide. Clearly, more testing experiments have to perform to find the best way to obtain reliable MI-VCD spectra.

## References

- 1 Hallam, H. E. *Vibrational Spectroscopy of Trapped Species*, A Wiley-interscience Publication: Toronto, **1973**.
- 2 King, S.H. *J. Phys. Chem.* **1970**, *74*, 2133.
- 3 Barnes, A.J. *Matrix Isolation Spectroscopy*, D. Reidel Publishing Company: Dordrecht, **1980**, Chapter 2.
- 4 Schlosser, D. W.; Devlin, F.; Jalkanen, K.; Stephens, P. J. *Chemical Physics Letters*, **1982**, *88*, 286.
- 5 Henderson, D.O.; Polavarapu, P.L. *J. Am. Chem. Soc.* **1986**, *108*, 7110.
- 6 Tarczay, G; Magyarfalvi, G; Vass, E. *Angew.Chem.Int.Ed.* **2006**, *45*, 1775.
- 7 Qu, X.; Citra, M.; Ragunathan, N.; Freedman, T. B.; Nafie, L. A. *Proceedings of the 9<sup>th</sup> International Conference on fourier Transform Spectroscopy*, SPIE Vol. 2089, 1993, p.142
- 8 Cao, X.; Dukor, R. K.; Nafie, L.A. *Theor. Chem. Account.* **2008**, *119*, 69.
- 9 Borba, A; Zavaglia, A. G; Fausto, R. *Vibrational spectroscopy*, **2004**, *36*, 79.
- 10 Han, S.W.; Kim, K. *J. Phys. Chem.* **1996**, *100*, 17124.

## Chapter 5 Conclusion

This thesis is a general summary of my graduate school work. The two projects I was involved are described in chapter 3 and chapter 4. Methyl lactate with several important functional groups, was used as a prototype molecule for the studies in carried out in carbon tetrachloride and in methanol, as well as in an argon matrix.

We have successfully determined the major species in the 2M methyl lactate solution in non-polar solvent  $\text{CCl}_4$  and in polar solvent  $\text{CH}_3\text{OH}$  using VA, VCD and DFT theoretical modeling. The unexpected blue shift of the  $\text{C}=\text{O}$  stretching band in  $\text{CH}_3\text{OH}$  compared to in  $\text{CCl}_4$  has been explained by modeling the explicit hydrogen-bonding between methyl lactate and one, two and three methanol molecules.

In order to achieve better spectral solution and also to “synthesize” the particular hydrogen-bonded complexes of interest, I started to construct an argon matrix isolation system in order to produce these targeted complexes. The argon matrix can not only avoid the solvent effect but also gives us a better control of what compositions of the complexes we have. For example, we can deposit the methyl lactate and water with a molar ratio of 1:1 and expect that if the 1:1 methyl lactate-methanol binary complex are the dominant clusters produced. This would

then allow direct comparison of experiments with the gas phase calculations and one may be able to draw more conclusive information. I have obtained some preliminary results with regard to this second project, although a number of challenges have been encountered. For example, it was very difficult to generate a smooth matrix film surface. The light source strength, the optical alignment, the matrix deposition period, and mixture deposition rate are all critical in achieving a good matrix sample. I have recorded both infrared and VCD spectra of the methyl lactate monomer in argon matrix, although the corresponding VCD spectra of the complexes of methyl lactate with methanol and water have yet to be obtained reliably. I expect that a new light source with more light output and a better sample mixing system will improve the experiments. Much more experimental efforts are needed in order to record reliable VCD spectra in matrix.